Supplement to

Super-Resolution Imaging of Multiple Cells by Optimised Flat-Field Epi-Illumination

Kyle M. Douglass, Christian Sieben, Anna Archetti, Ambroise Lambert, and Suliana Manley

Institute of Physics, École Polytechnique Fédérale de Lausanne (EPFL),

Route Cantonale, 1015 Lausanne, Switzerland

Corresponding authors: Kyle M. Douglass (kyle.douglass@epfl.ch) and Suliana Manley (suliana.manley@epfl.ch)

TABLE OF CONTENTS

2. Supplementary Data

3. FIFI Optics

5. Field-Dependent Direct STORM Simulations

1. SUPPLEMENTARY FIGURES

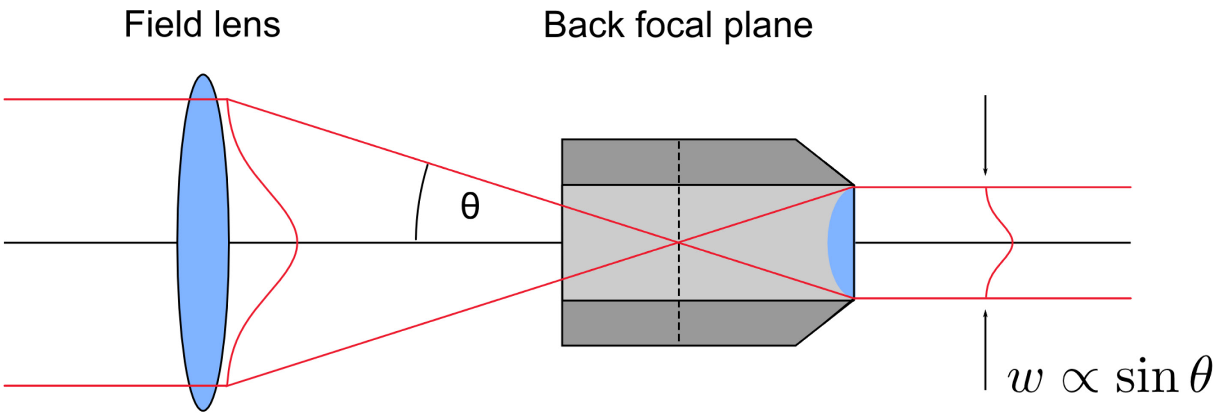

Supplementary Figure 1 Widefield laser epi-illumination delivers a Gaussian beam profile to the sample. The width of the beam on the sample is proportional to the angular width of the input beam.

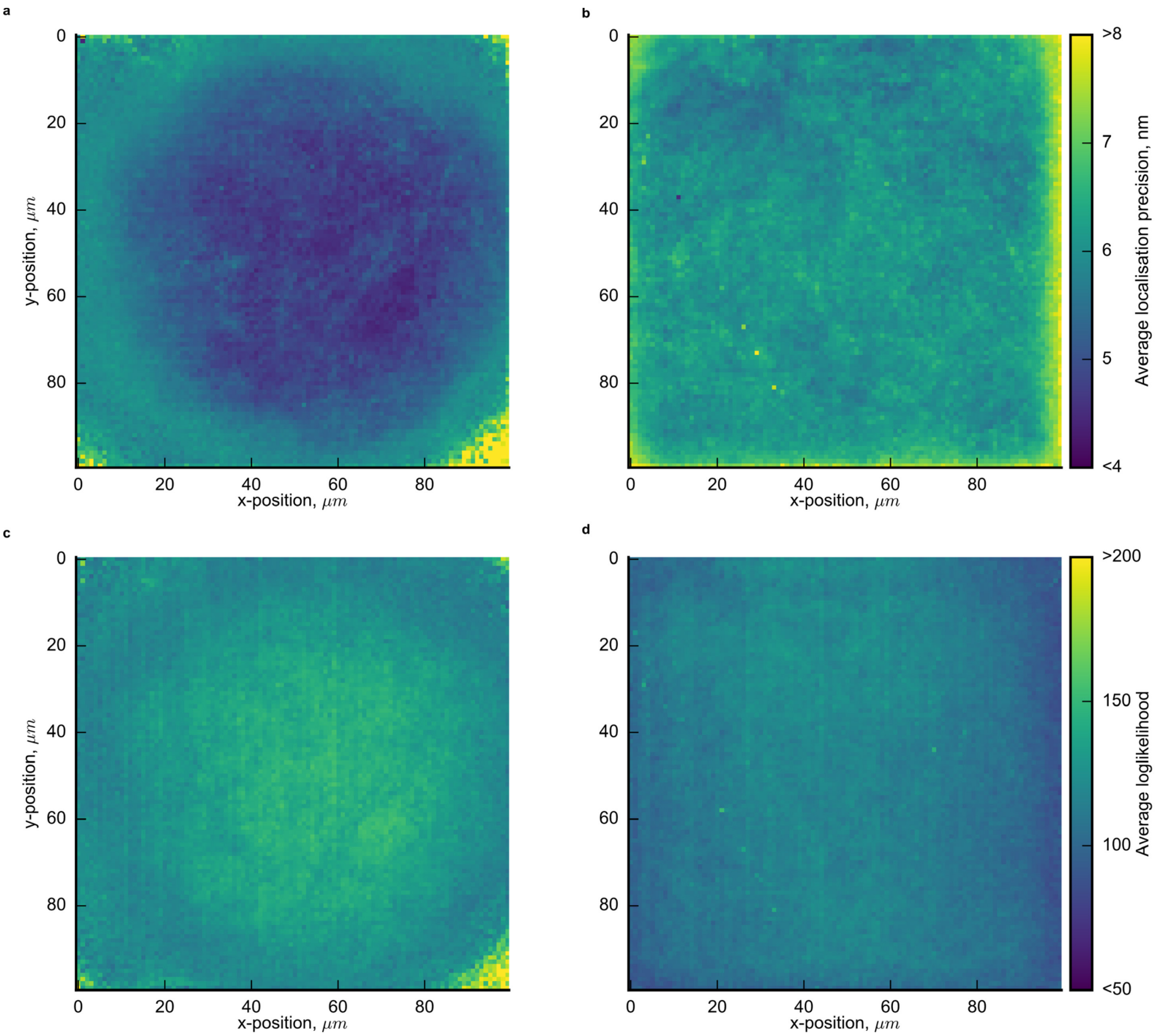

Supplementary Figure 2 Field dependence of experimental SMLM image quality parameters for a Gaussian beam and flat illumination. Binned and averaged localisation precision for **a)** Gaussian illumination and **b)** flat-field illumination for the data in Fig. 1. The localisation precision quantifies the precision in the fluorophores' position estimates and depends, among other factors, on the number of emitted photons[1]. Lower values indicate better precision. Binned and averaged loglikelihood ratio for **c)** Gaussian illumination and **d)** flat-field illumination. The loglikelihood ratio is a goodness-of-fit measure of how well a localisation matches the expected shape of the microscope's point-spread function—which here is assumed to be Gaussian—and tends towards a chi-squared distribution[2]. Besides the shape of the single molecule image, the loglikelihood ratio also depends on the camera read noise and the photon shot noise. The latter includes laser light leakage through the dichroic in the regions of high laser irradiance. Lower values indicate better fits. Both parameters are computed by the localisation algorithm used in this work[3].

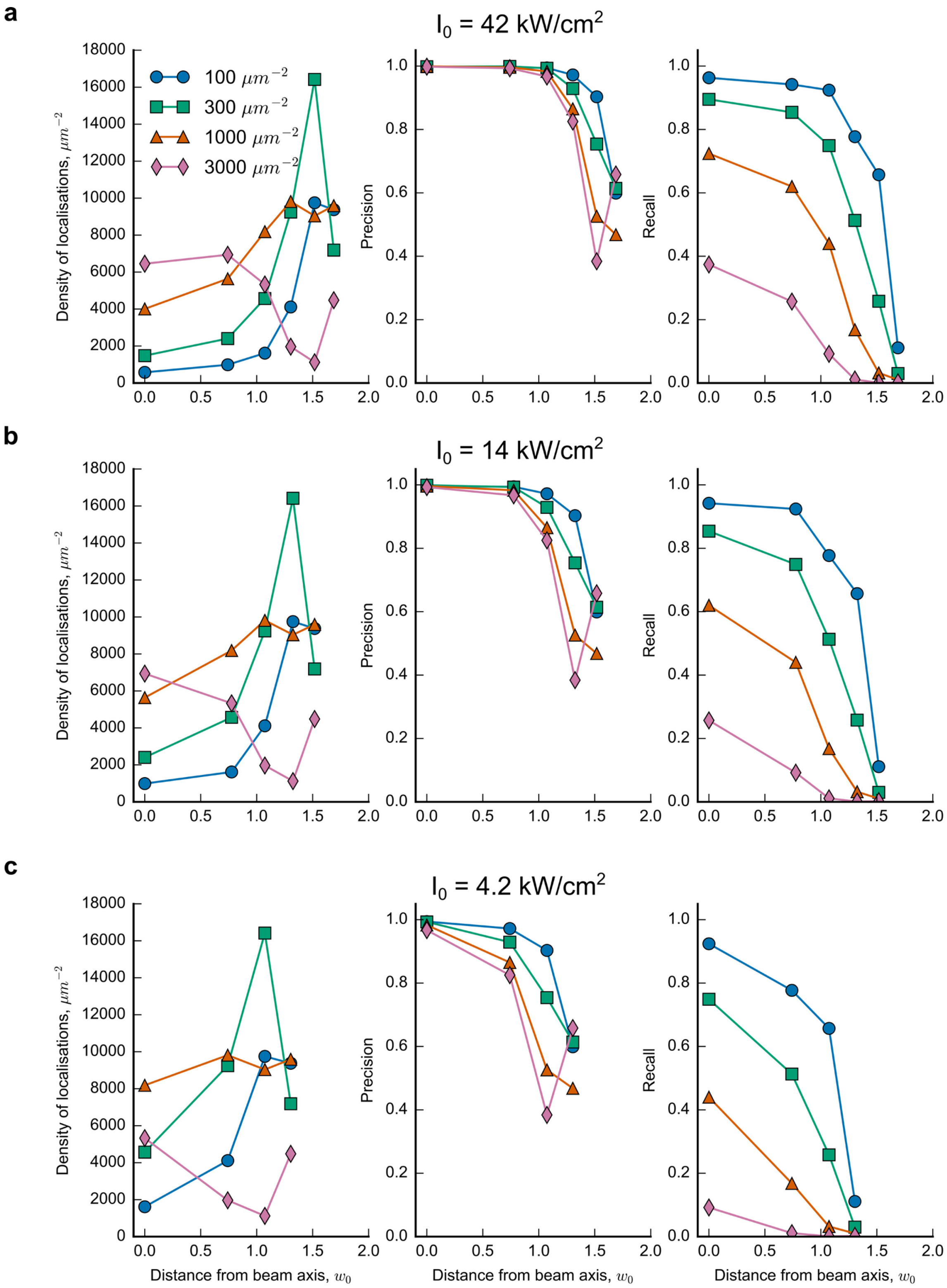

Supplementary Figure 3 Simulations of a 2D direct STORM experiment of a surface uniformly labelled with fluorophores under Gaussian beam epi-illumination with beam waist radius w_0. Gaussian peak irradiance is $42\ kW/cm^2$, $14\ kW/cm^2$, and $4.2\ kW/cm^2$ in **a**, **b** and **c**, respectively. The legend in **a**

applies to all plots and denotes the simulated fluorophore density. Discussion of these results is found in the Supplementary Text starting on page 43.

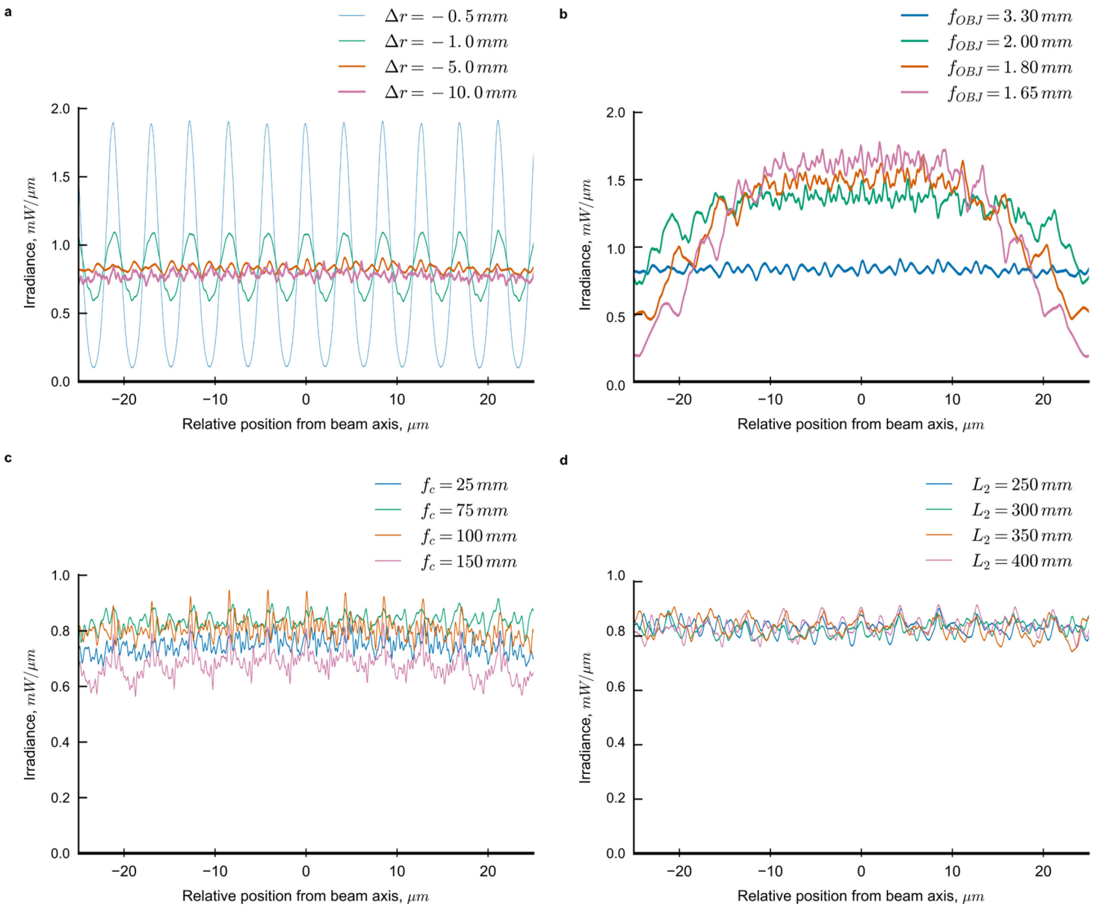

Supplementary Figure 4 Zoomed plots of the central regions of profiles shown in **Fig. 3** of the main text.

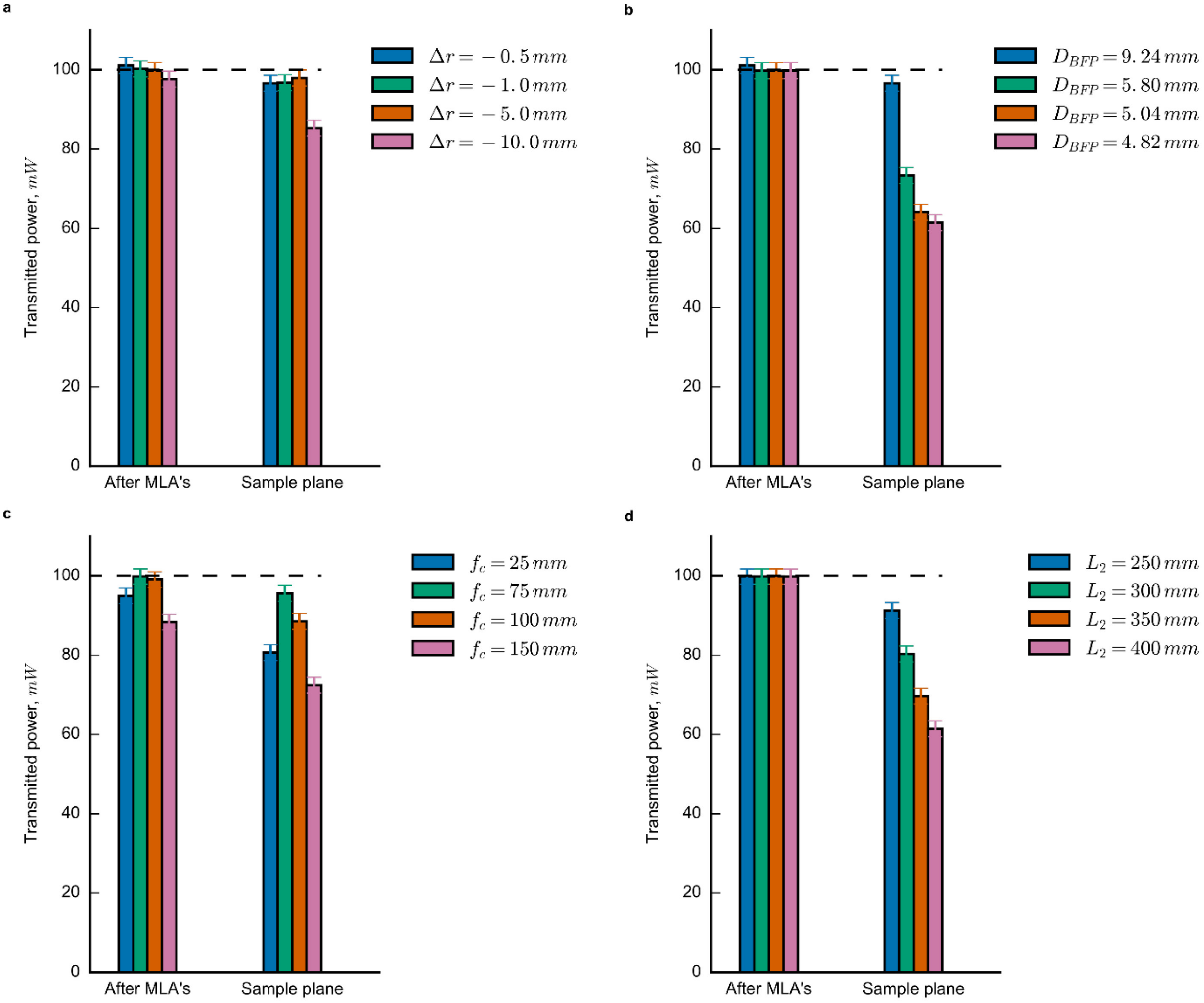

Supplementary Figure 5 1D simulations of the transmitted power from a 100 mW input Gaussian beam through the FIFI system for various design parameters at the planes $u_2(x)$ and $u_4(x)$ marked in Fig. 2. **a)** Repositioning the rotating diffuser does not lead to large losses in power except for large diffuser offsets. **b)** Using an objective with a small BFP diameter leads to significant loss of light. The objectives simulated here correspond to the same ones simulated in Fig. 3b. **c)** Transmitted power as a function of the collimating lens focal length. **d)** Increasing the distance between the MLA's and the objective lens results in loss of power due to overfilling the BFP. Error bars: +/- 2 mW, which is the maximum observed deviation of the power when a system with no loss is simulated. All simulation parameters are described in Supplementary Table 1.

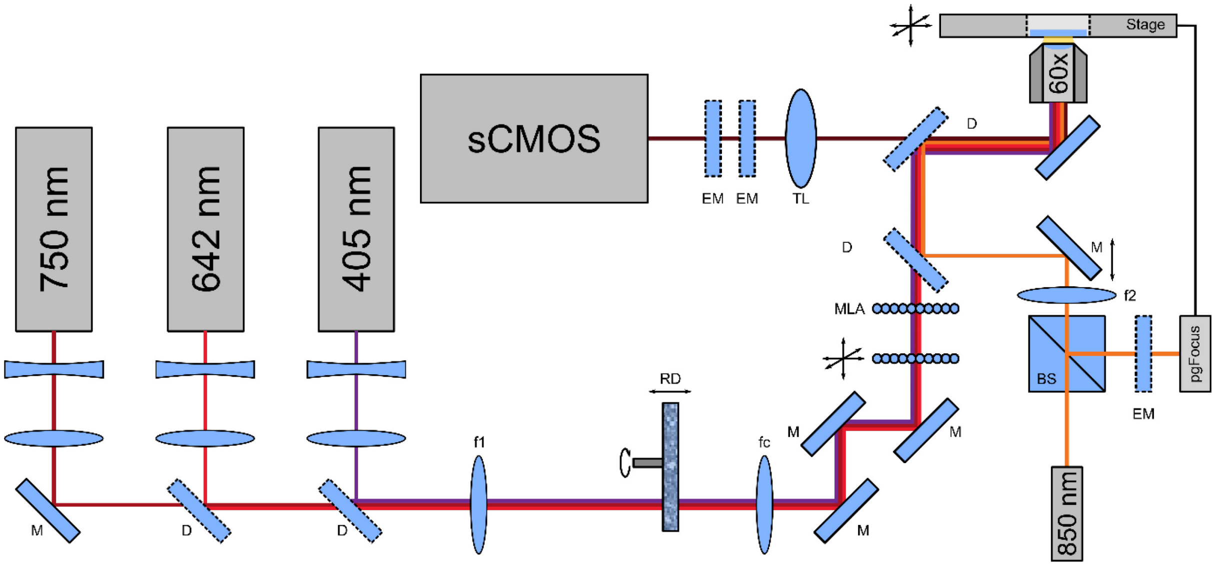

Supplementary Figure 6 Custom-built STORM microscope utilizing the FIFI epi-illumination system. The laser beams are expanded and combined using a mirror (M) and dichroics (D) before being launched into the telescope. The axial position of the rotating diffuser (RD) may be manually adjusted to tune the modulation of the grating diffraction peaks from the MLA's. The MLA's are mounted on x-y fine adjustment mounts and may be coarsely adjusted along the axial direction to change the size of the illuminated area. Fluorescence light is collected by the objective lens and imaged onto the sCMOS camera using a tube lens (TL) and fluorescence emission filters (EM). A 850 nm IR laser diode is reflected off the coverslip in total internal reflection and its position monitored with the pgFocus open hardware autofocus system to actively correct axial drift. BS – beam splitter.

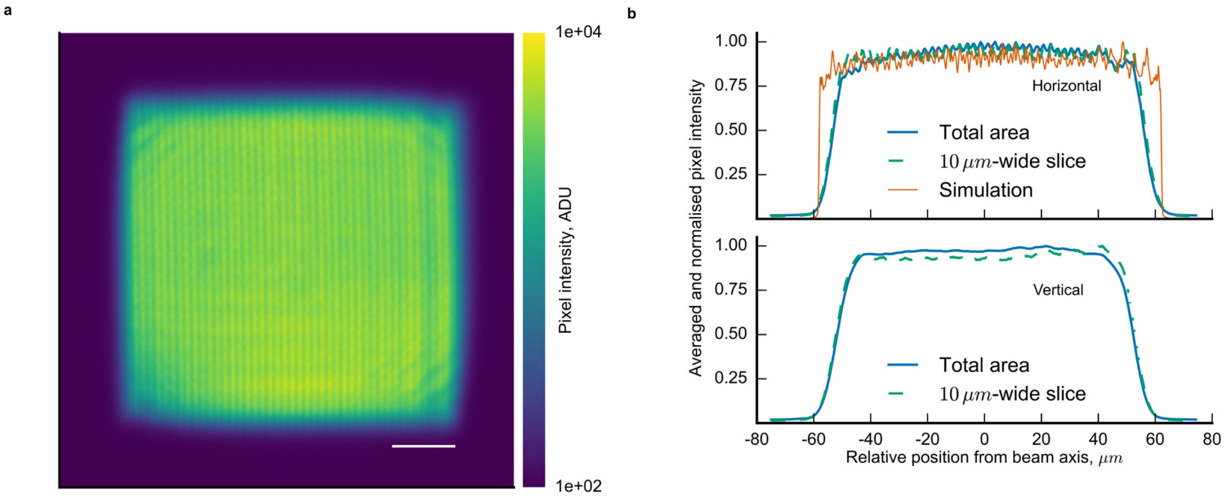

Supplementary Figure 7 Illumination profile of the 642 nm laser in the sample plane by imaging fluorescence from a dense solution of acid blue #9 (AB9). **a)** Image averaged over nine different fields of view. **b)** Horizontal and vertical line profiles through the image in a. The slices were taken from the centre of the image. The signal comes from a concentrated solution of Acid Blue #9 on the coverslip. Camera integration time was 200 ms; approximately 1.4 mW of power was illuminating the sample. Scale bar: 20 μm.

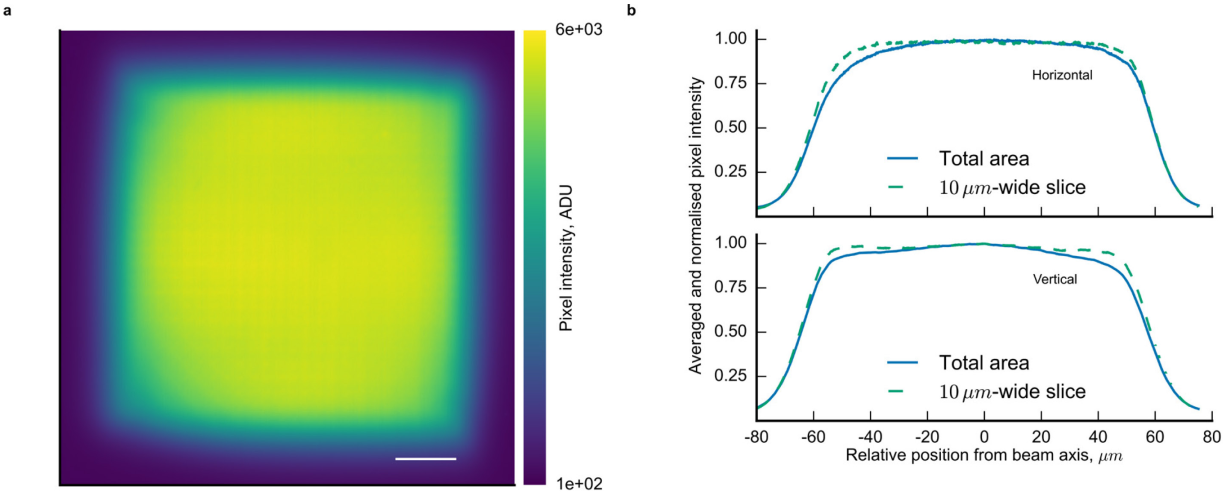

Supplementary Figure 8 Illumination profile of the 750 nm laser in the sample plane by imaging fluorescence from a dense solution of acid blue #9 (AB9). **a)** Image averaged over nine different fields of view. **b)** Horizontal and vertical line profiles through the image in a. The slices were taken from the centre of the image. The signal comes from a concentrated solution of Acid Blue #9 on the coverslip. Camera integration times were increased to 1000 ms and the laser power was decreased to approximately 0.3 mW to increase signal-to-noise and reduce artefacts in the homogeneity due to out-of-focus fluorescence. Scale bar: 20 µm.

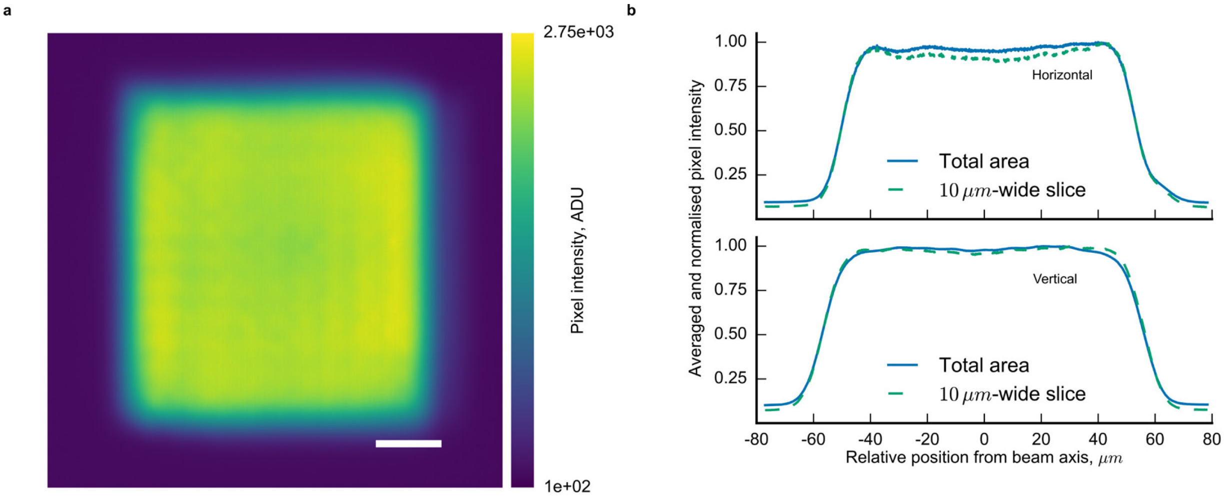

Supplementary Figure 9 Illumination profile of the 405 nm laser in the sample plane by imaging fluorescence from a dense solution of acid blue #9. **a)** Image averaged over nine different fields of view. **b)** Horizontal and vertical line profiles through the image in a. The slices were taken from the centre of the image. The signal comes from a concentrated solution of Acid Blue #9 on the coverslip. Camera integration times were set to 100 ms and the laser power was decreased to approximately 1 mW to increase signal-to-noise and reduce artefacts in the homogeneity due to out-of-focus fluorescence. Scale bar: 20 μm.

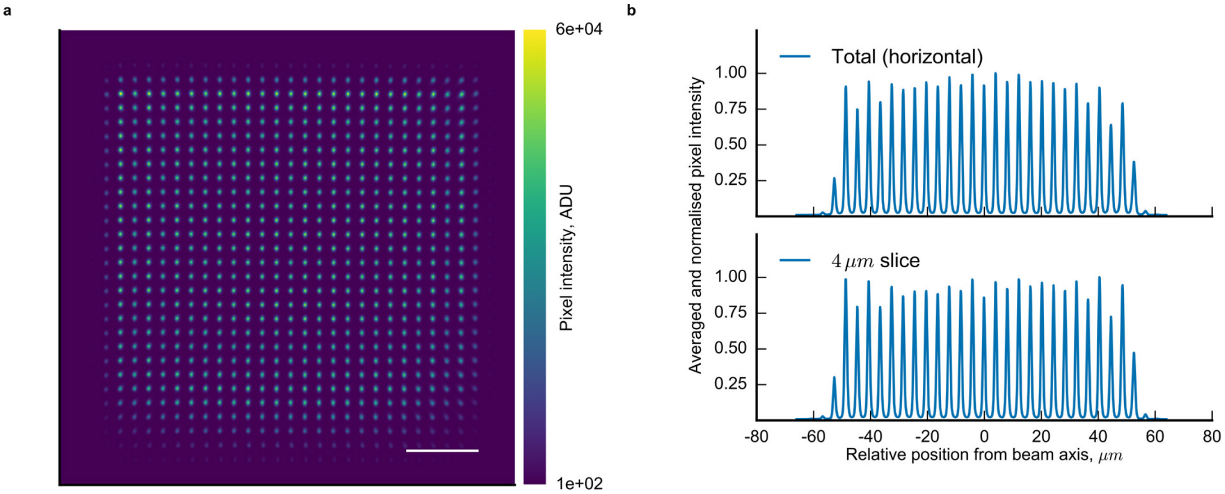

Supplementary Figure 10 Grating diffraction observed in the experimental sample plane irradiance by removing the rotating diffuser from the setup. **a)** Average irradiance from nine fields of view. **b)** Integrated horizontal line profile and a profile through one line of spots. The signal comes from fluorescence excited by a 642 nm laser light in a thick, highly concentrated dye solution of Acid Blue #9 on a coverslip. According to Fig. 2 in the main text, the pattern can be interpreted as the result of interference between the independently propagating beamlets traveling at different angles to the optics axis in the sample plane. Scale bar: 20 μm.

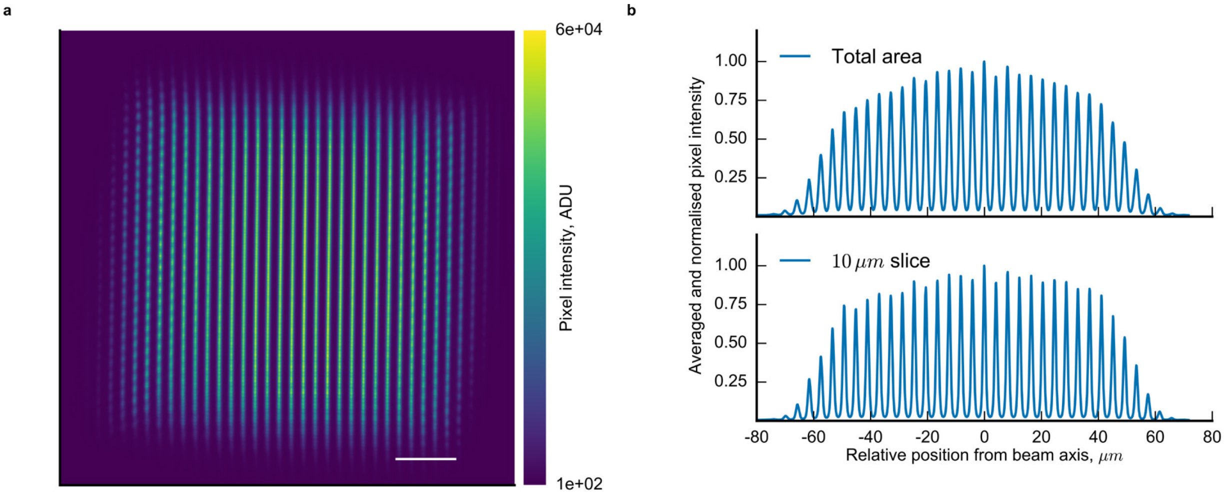

Supplementary Figure 11 Experimental sample plane irradiance from the epi-illumination system with the diffuser placed exactly in the focal plane of the collimating lens and a primary dichroic possessing an unintentional slight curvature in one direction. The vertical lines arise from defocusing of the array profile out of the sample plane in one direction. This figure demonstrates that the diffuser does little to eliminate the grating artefacts if not properly placed. It also demonstrates that aberrations like astigmatism in the incoming beam can smooth over inhomogeneities in the illumination profile. Scale bar: 20 µm.

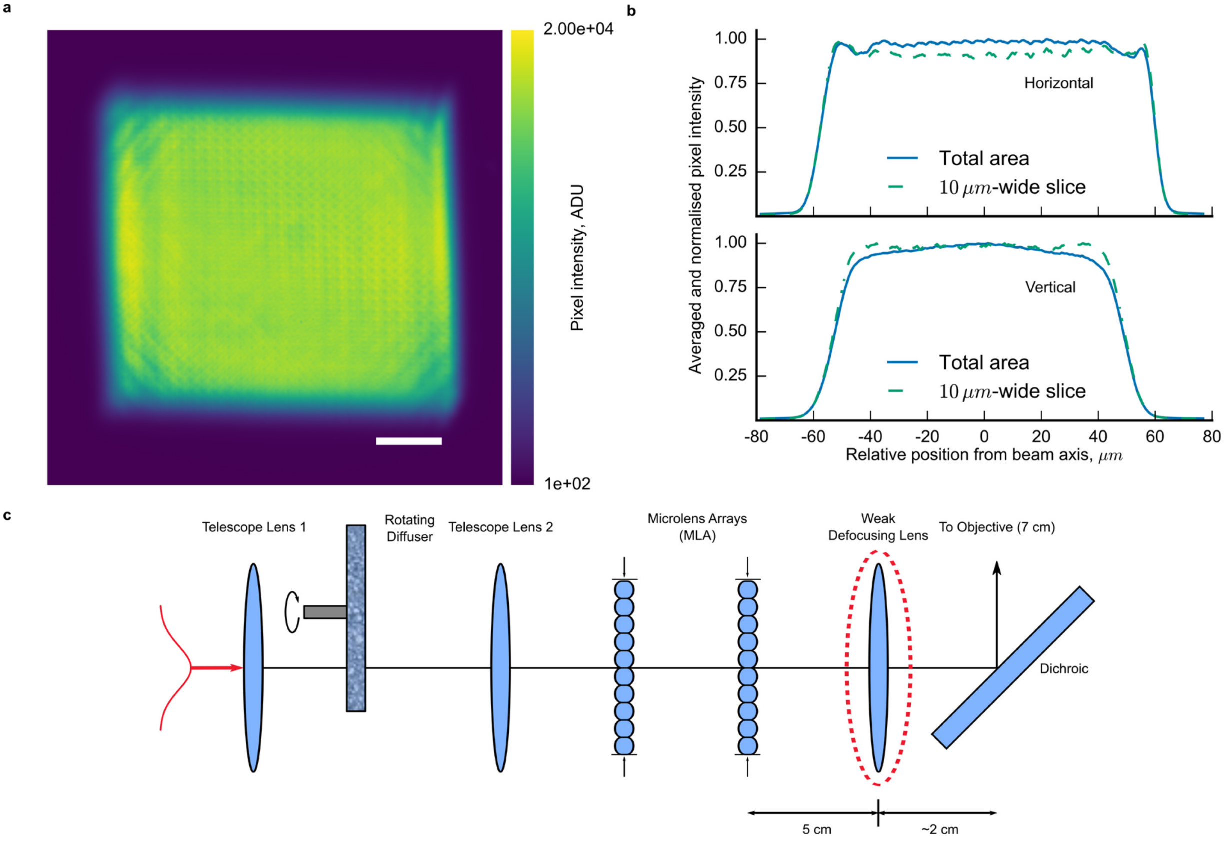

Supplementary Figure 12 Defocusing the illumination reduces the residual grating artefacts in the illuminated region. **a,b** Fluorescence signal and horizontal and vertical line profiles from 642 nm excitation. **c** A f = +400 mm cylindrical lens (Thorlabs LJ1363RM-A) was inserted into the excitation path of the dichroic cube (Thorlabs DFM1/M) between the second microlens array and the objective with its axis perpendicular to the curved axis of the dichroic. This slightly defocused the vertical stripes in the 642 nm profile (Supp. Fig. 7) out of the sample plane at the cost of a smaller vertical extent of the illuminated region. Defocus in the other transverse direction was induced by the curved dichroic (Supp. Fig. 11). Camera integration time was 100 ms. Sample plane laser powers was approximately 1.4 mW. Scale bar: 20 µm.

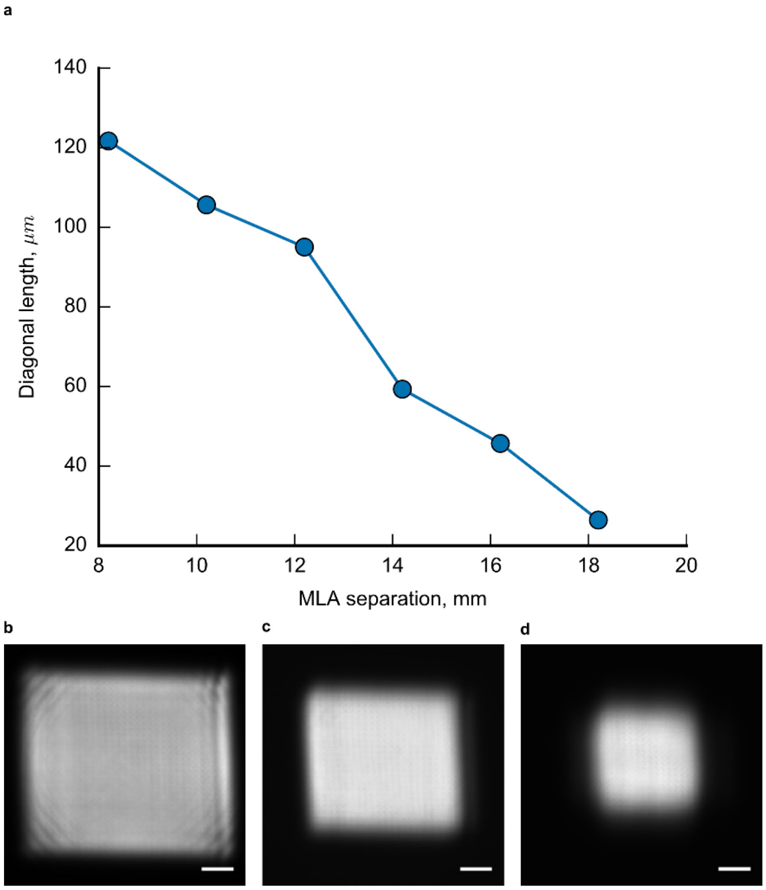

Supplementary Figure 13 The size of the flat-illuminated region on the sample is continuously variable over nearly an order of magnitude. **a** The average length of the two diagonals across the illuminated region and its dependence on the separation between the microlens arrays (MLA). The length of each diagonal was measured by taking a line profile through the image of the fluorescence signal from a dense solution of Acid Blue #9 deposited on a coverslip and excited by 642 nm light (Methods). The diagonal length is defined here as the length of the section of the diagonal that spans the region where the fluorescence intensity remains between 90% and 100% of the maximum value. No clipping of the beam is required to change the size, so the total power delivered to the sample remains constant for all the above sizes. **b—d** Images of the fluorescence signal from the Acid Blue #9 solution for MLA separations of 8, 12, and 16 mm, respectively. Scale bars: 20 μm.

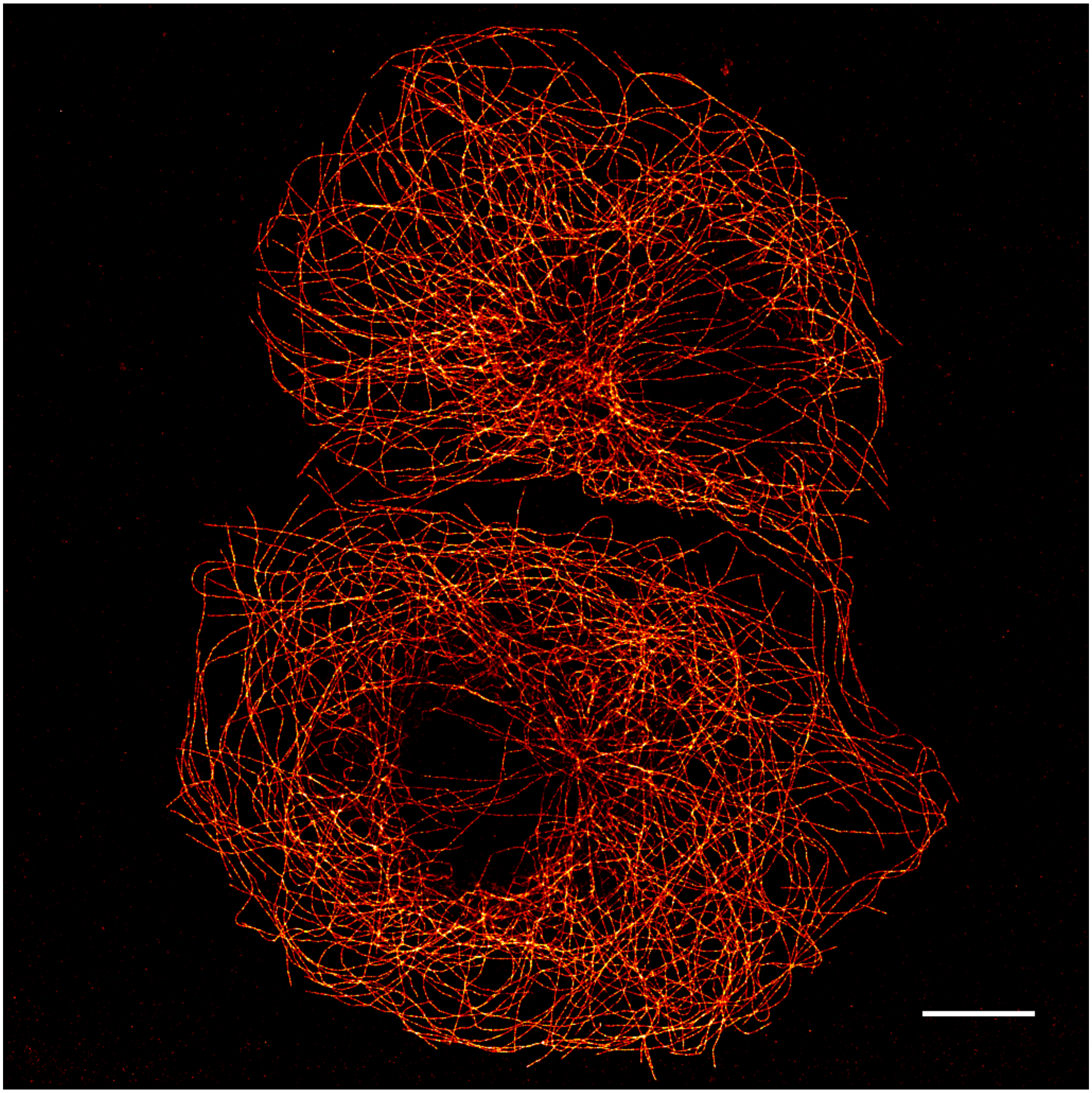

Supplementary Figure 14 STORM image of microtubules in COS7 cells. Cells were labelled with antibodies against α-tubulin and secondary antibodies conjugated with AlexaFluor 647. Scale bar 10 μm.

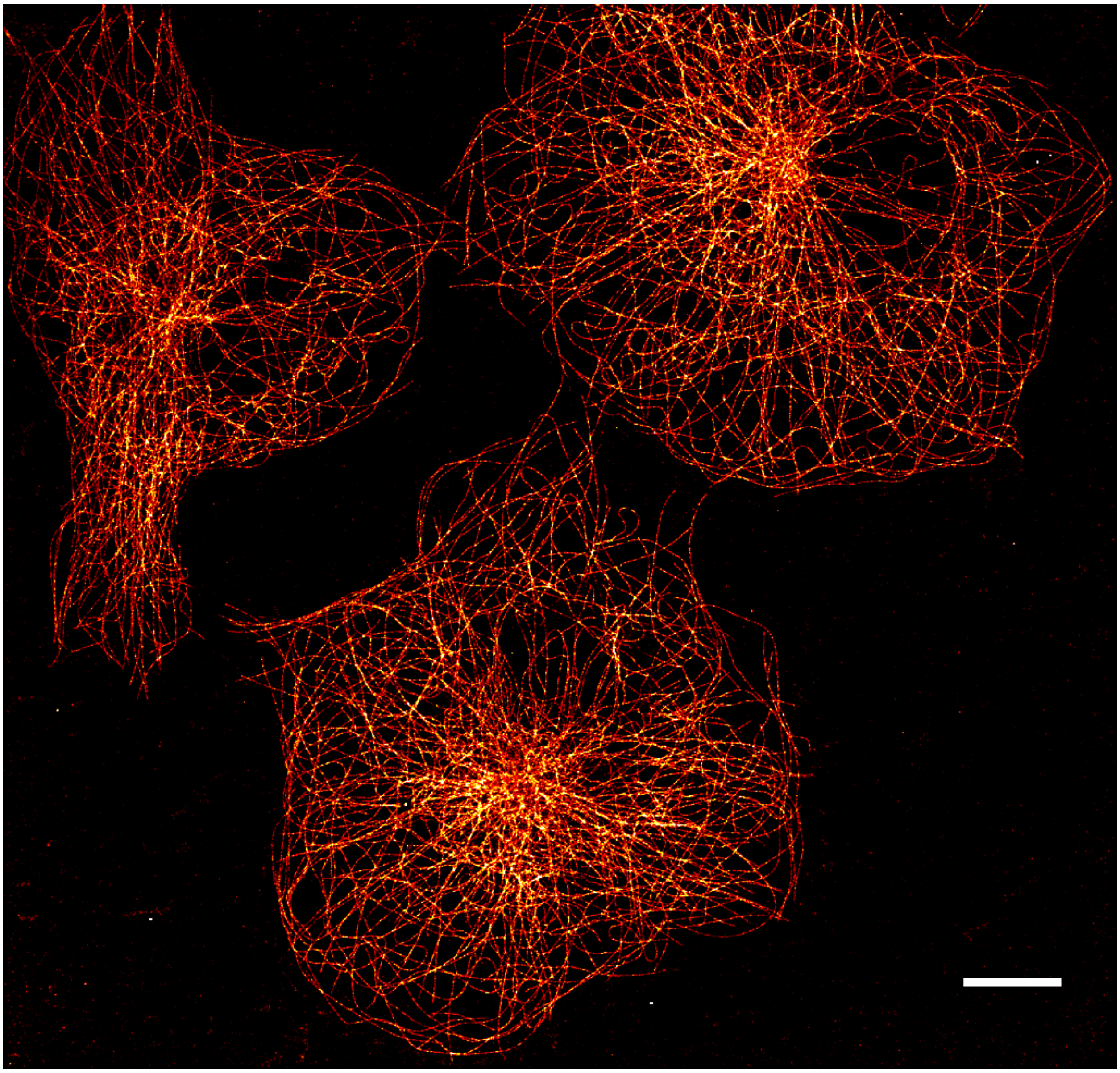

Supplementary Figure 15 STORM image of microtubules in COS7 cells. Cells were labelled with antibodies against α-tubulin and secondary antibodies conjugated with AlexaFluor 647. Scale bar 10 µm.

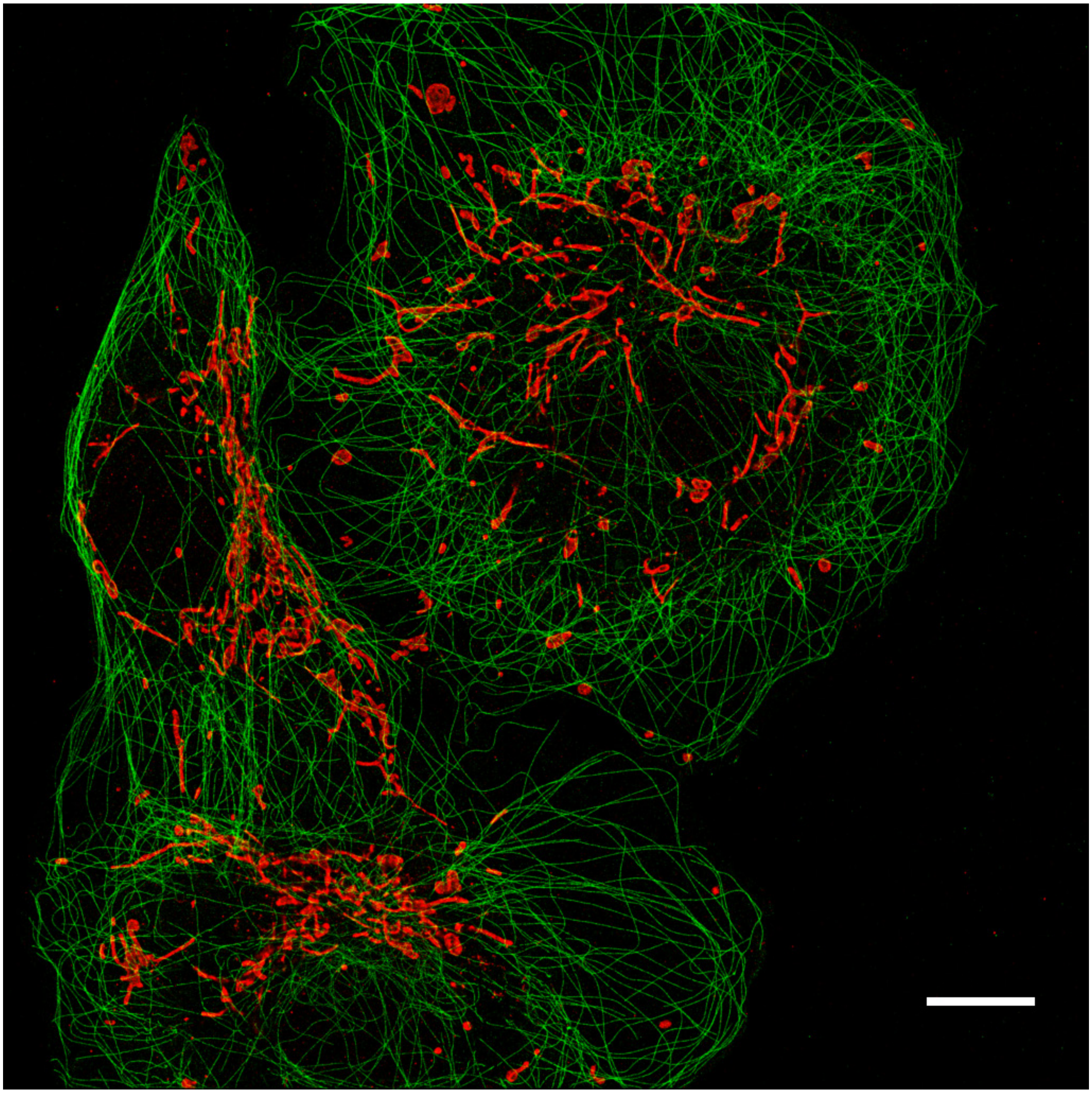

Supplementary Figure 16 Two-colour STORM image of microtubules and mitochondria in Cos7 cells. Cells were labelled with antibodies against α-tubulin and TOM20, which were visualized using secondary antibodies conjugated with AlexaFluor 647 (microtubules, green) and AlexaFluor750 (mitochondria, red). Scale bar: 10 μm.

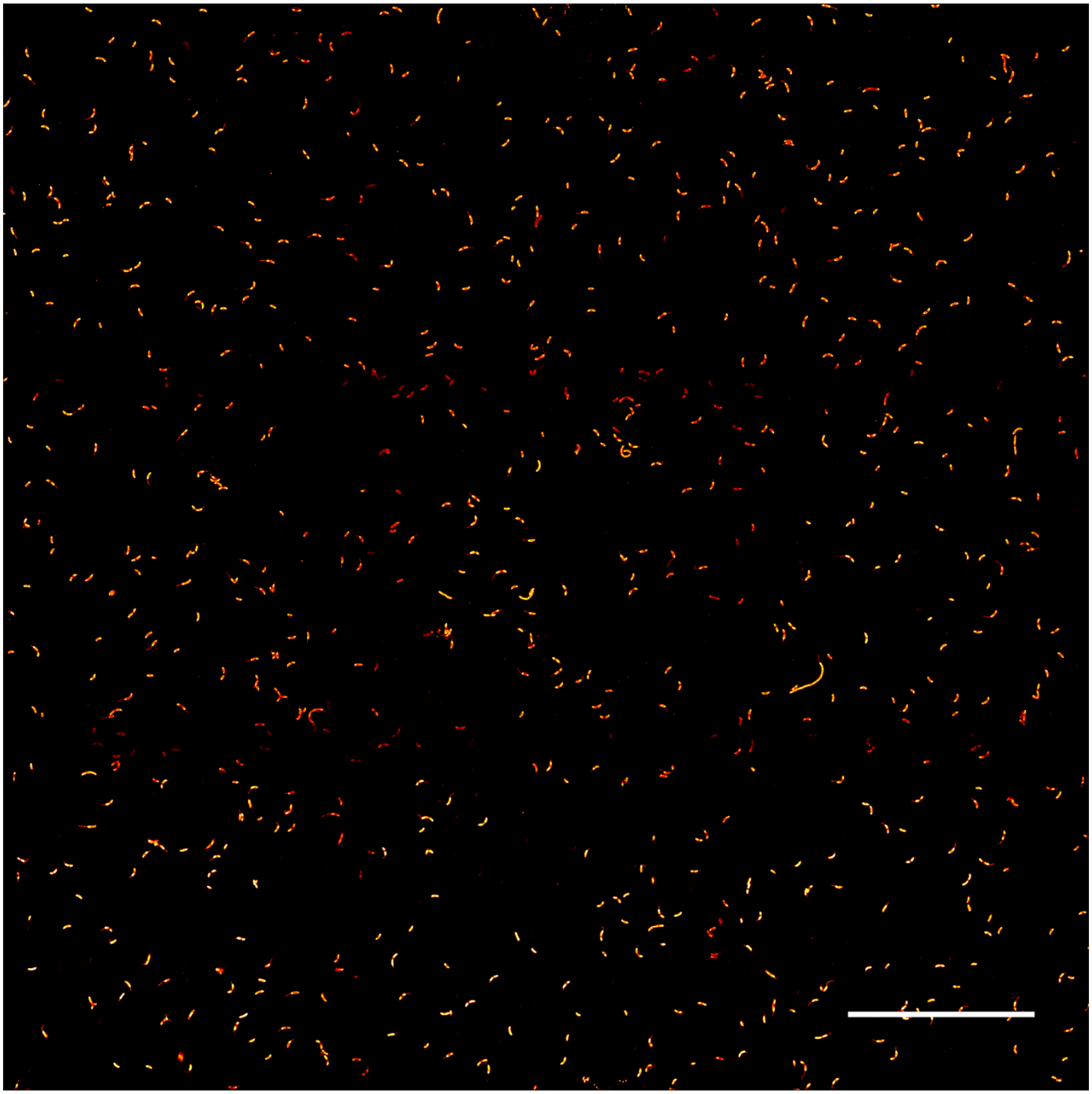

Supplementary Figure 17 STORM image of *Caulobacter crescentus* CB15N cell wall. Image was stitched together from 9 different FOVs using the Stitching 2D/3D Plugin in FIJI. Bacteria cells are labelled with WGA-AlexaFluor 647 conjugate. Scale bar: 50 µm.

2. SUPPLEMENTARY DATA

Wave Optics Simulation Parameters

	Units	**Panel a**	**Panel b**	**Panel c**	**Panel d**
Δr, Diffuser offset	mm	See figure	-0.5	-0.5	-0.5
f_{OBJ}, Objective focal length	mm	3.3	See figure	3.3	3.3
D_{BFP}, objective BFP diameter	mm	9.24	See figure	9.24	9.24
f_c, collimating lens focal length	mm	50	50	See figure	50
L_2, Distance between second MLA and objective BFP	mm	200	200	200	See figure
p, Lenslet periodicity	µm	500	500	500	500
N, number of lenslets	n.a.	21	21	21	21
f_{MLA}, lenslet focal length	mm	13.7	13.7	13.7	13.7
L_1, distance between collimating lens and MLA's	mm	750	750	750	750
λ, wavelength	nm	642	642	642	642
σ_f, diffuser correlation length	µm	10	10	10	10
σ_r, diffuser variance	n.a.	1.75	1.75	1.75	1.75
σ, beam standard deviation at waist	µm	6	6	6	6
nIter, Number of field realizations	n.a.	1000	1000	1000	1000
Input beam grid size	n.a.	20001	20001	20001	20001
Input beam grid physical size	mm	5	5	5	5
MLA grid size	n.a.	420,021	420,021	420,021	420,021
MLA grid zero padding	n.a.	840,042	840,042	840,042	840,042
BFP grid size	n.a.	420,021	420,021	420,021	420,021
BFP grid zero padding	n.a.	1,680,084	1,680,084	1,680,084	1,680,084

Table 1 Simulation parameters for Fig. 3 of the main text and Supplementary Fig. 3 and 4.

Transmitted Power Measurements

The fractions of the transmitted laser power through the system illustrated in Supp. Fig. 6 were measured with a Thorlabs PM100A power meter and Thorlabs S302C thermal sensor. At points where the laser beam would overfill the sensor, a f = +75 mm plano-convex lens was placed in front of it to capture all of the power and focus the beam onto the sensor. Otherwise, the power meter was placed directly in the beam path.

Position	**Power @ 642 nm, mW**	**Power @ 750 nm, mW**
Laser output	1.87 ± 0.01	48.4 ± 0.2
After the telescope (with diffuser)	1.58 ± 0.01	41.1 ± 0.1
After the telescope (without diffuser)	1.77 ± 0.01	43.0 ± 0.1
Objective BFP (with MLAs)	1.35 ± 0.01	33.4 ± 0.2
Objective BFP (without MLAs)	1.45 ± 0.01	37.5 ± 0.1

Table 2 Measurements of optical power made at different locations along the laser beam path.

The total fraction of power transmitted to the objective's BFP is $1.35/1.87 = 0.723$ at 642 nm. At 750 nm, it is practically equivalent: $33.4/48.4 = 0.690$.

The diffuser accounts for approximately 4% to 11% of the losses. The transmittance of the two MLAs is approximately 89% to 93%; the remaining losses come from the dichroics and reflections and/or scattering from the other optics. Because the losses come from passive elements, we don't expect them to change at the higher laser powers used in the experiments.

3. FIFI OPTICS

Alignment Guide

Before starting, we assume that you already have a working widefield laser epi-illumination microscope with laser lines that are well-collimated and collinear. This alignment does not require an open stage like the ASI-RAMM that is used in our setup (see Methods), though you will need to remove the field lens (Supp. Fig. 1) if working with a commercial microscope body. Furthermore, we assume that you already have determined the positions for the rough placement of the telescope lenses, the second lens focal length (f_c), diffuser offset (parameter Δr), and second MLA position before the objective (L_2) using the SimMLA software package (Methods) or otherwise. Finally, you should have the following standard optics lab equipment:

1. Irises and their posts and mounts
2. A shearing interferometer (such as Thorlabs SI035 or SI050) for axial lens alignment
3. Cage rods, cage plates, a lens tube, and additional irises to aid vertical alignment.

In the figures that follow, we have removed all unnecessary items and drawn the microscope as a “standard” laser epi-illumination fluorescence microscope. The main components of this system before modification are the field lens, the dichroic, and the objective. The vertical section consisting of the space above the dichroic has been rotated into the plane of the sketch for ease of visualization.

Unless otherwise noted, all mirrors are mounted in tip-tilt micrometre mounts for precision beam steering, such as Thorlabs KMS/M. Lenses are mounted in transverse, two-axis kinematic mounts (Thorlabs LM1XY). Our dichroic is mounted in a Thorlabs DFM1/M fluorescence filter cube, which is similar to many other commercial filter cubes. Care should be taken to ensure that the dichroic is oriented at 45 degrees to the table so that the incoming and outgoing beams from the cube can be made as horizontal and vertical to the table as possible, respectively. Mounting the dichroic holder on a rotation stage or tip-tilt stage can ensure this.

As a final note, all beam shaping techniques require a good quality input beam to work, and FIFI is no exception. When we tested a high power diode laser with a beam quality factor of $M^2 \approx 22$ we could not obtain a uniform illumination, nor could we easily prevent overfilling of the objective back aperture. The lowest quality laser mentioned in the manuscript (Methods) in terms of beam quality factor was the Coherent Obis 405 nm whose manufacturer specification is $M^2 \leq 1.3$; since this laser produced a smooth profile (Supp. Fig. 9), we expect that lasers with beam quality factors equal to or smaller than this should work with FIFI.

WARNING: Aligning optical systems using lasers is inherently dangerous and carries a risk of significant eye and/or skin damage. Seek assistance from a safety officer or professional in optics before conducting this alignment.

Step 1: Remove the field lens and objective from the epi-illumination path

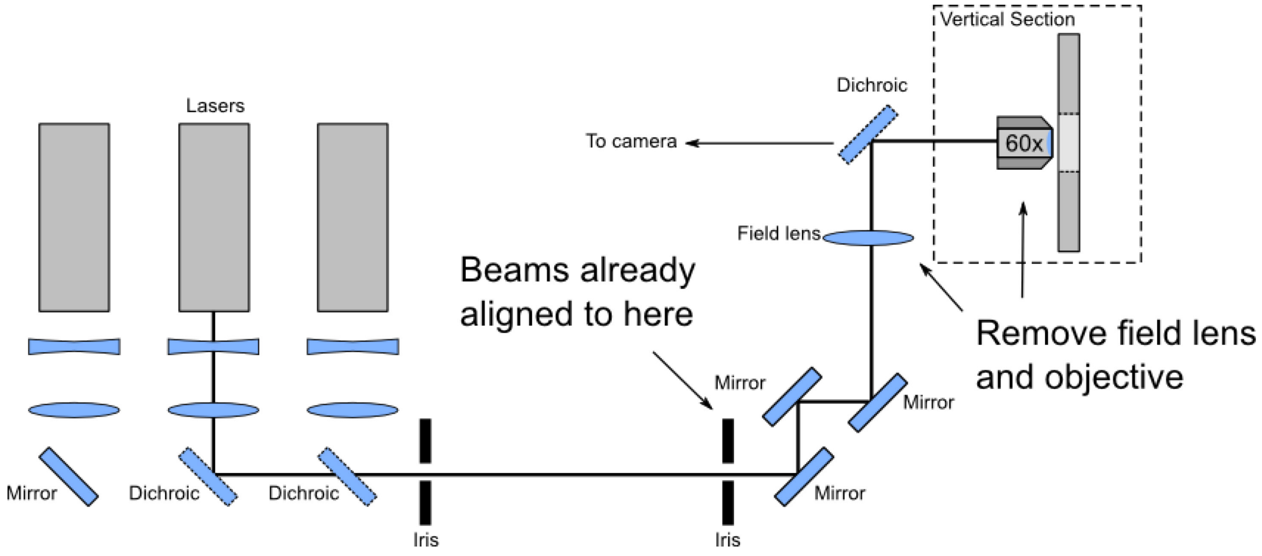

Step 2: Insert the vertical alignment tool into the objective port

For this step we use a simple, custom-made tool constructed from Thorlabs cage rods, irises, 2-inch cage plates, and a 1” lens tube that threads directly into the objective port via a thread adapter (Thorlabs SM1A11). The open design of the alignment tool allows you to see whether the beam is passing through both irises.

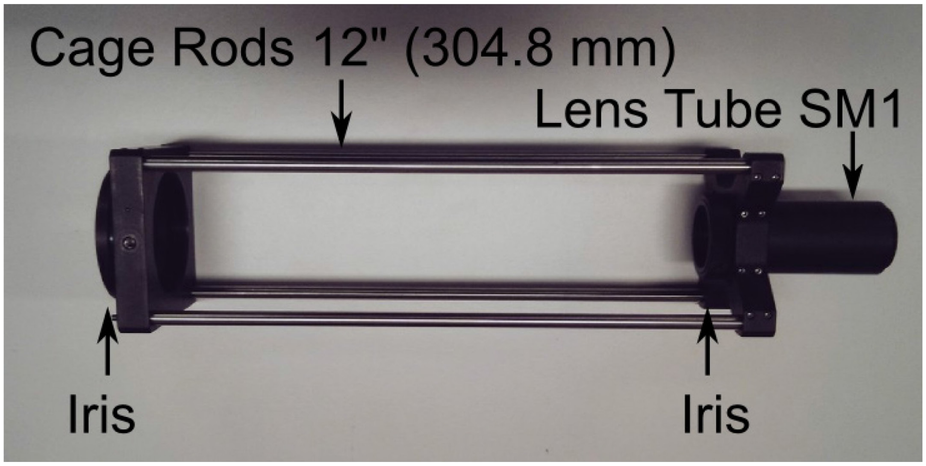

The vertical alignment tool threads directly into the microscope objective port and provides two irises centred on the optics axis.

Step 3: Align the laser to the irises in the epi-illumination path and vertical alignment tool

WARNING: Be very careful during this step as the laser will be traveling vertically relative to the table.

Turn on a laser and set it to a very low power (less than a milliWatt). Place two irises into the horizontal beam path between the mirrors and the dichroic at the same height as the beam coming from the lasers. You can ensure that the irises lie on a line by mounting them in posts that are screwed directly into the holes on the optical breadboard table. Collars (Thorlabs R2M) help when swapping posts between holders.

Turn the micrometre screws on the two mirrors in the figure to align the beam in both the horizontal and vertical directions, ensuring that the beam passes through all four irises. Typically, we align the horizontal path first, and then check the vertical alignment. You may need to adjust the dichroic position or angle to get the beam coaligned to both paths. You may also find that stopping down the iris closest to the lasers helps in producing a small beam diameter for downstream alignment.

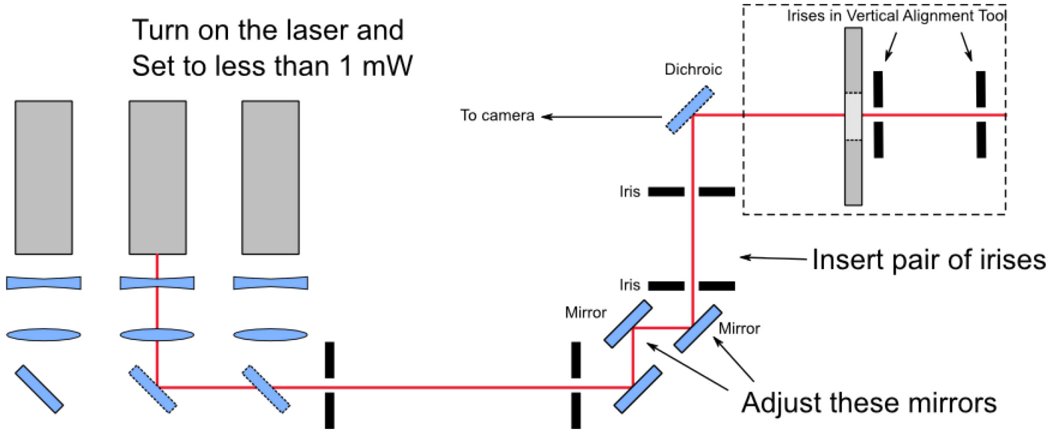
Turn on the laser and
Set to less than 1 mW

Insert pair of irises

Adjust these mirrors

Step 4: Insert the first telescope lens and align it

Place an iris (or pinhole if your focused beam is very small) at the same height as the laser beam in the position marked in the figure below. Insert the first lens of the telescope and adjust its x- and y-micrometre screws until the focus of the beam passes through the iris.

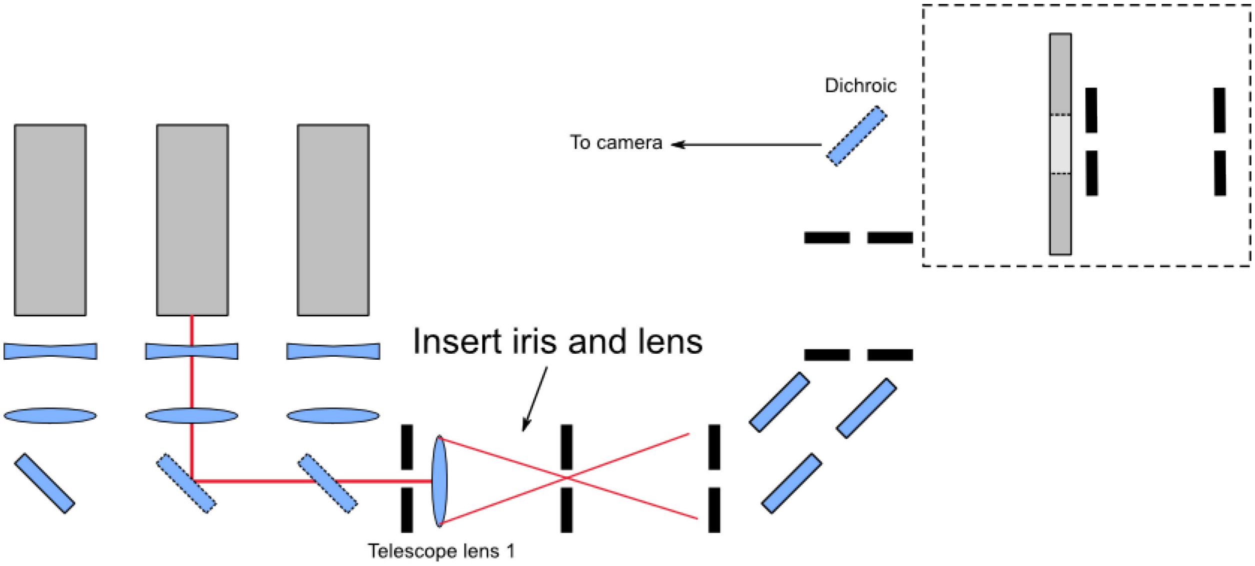

Step 5: Insert the second telescope lens and align it

Remove the iris inserted in the last step. Insert the second telescope lens (the collimating lens) and adjust its transverse position until the laser passes through all the irises. Use the shear plate to ensure that the beam is still collimated after the telescope by adjusting its axial position.

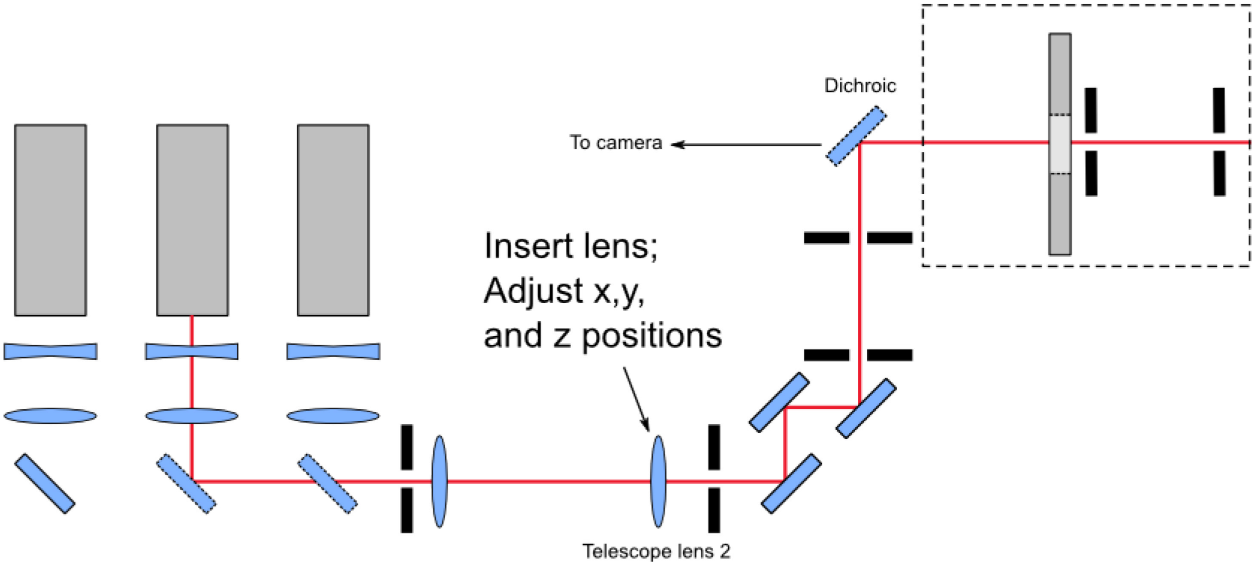

Step 6: Insert the microlenses and roughly align them axially and transversally

Now you can open the irises completely and remove the vertical alignment tool. (It's useful to keep the irises in the beam path for future realignments.) Insert the pair of microlenses into the beam path. You can centre them to the path by eye; no fine positioning is required. Their axial position should be that determined by your design. The relative distance between MLA's should be set to about one lenslet focal length to start. In general, it's best to place the MLA pair as close to the dichroic as possible to prevent the diverging beam from overfilling the objective back aperture. Reinsert the objective into the setup.

We mount the MLA's in 2 axis transverse kinematic mounts (Qioptiq G061025000) that are themselves placed in an axial cage system. The mounts allow us to align the MLA's relative to one another in directions transverse to the optics axis; the cage system lets us easily reposition the first MLA along the axial direction to change the beam size on the sample.

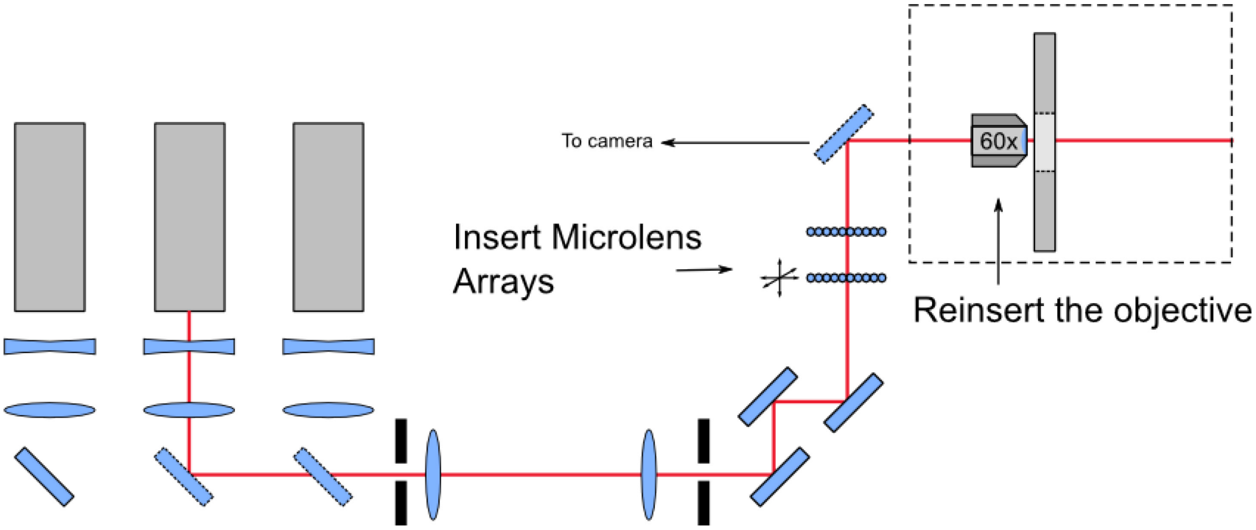

Step 7: Place a dye sample on the stage and focus on it

To finish the alignment, use a live image stream from a dye sample such as the one discussed in the Methods. For 642 nm light, a dense solution of Acid Blue #9 sandwiched between two coverslips will suffice.

Place the sample on the stage and adjust the focus until you see an image that should appear very roughly like Supp. Fig. 10. If you don't see distinct peaks, try coarsely adjusting the relative rotation of one of the MLA's about the optics axis; we do this by rotating the first MLA by hand within its mount.

Step 8: Insert the diffuser and align it axially

Insert the rotating diffuser close to the shared focal planes of the telescope lenses. (You may want to cover it in a shroud to prevent light scattering into the room.) Turn it on, then slide it back and forth along the axial direction while observing the illuminated region in the video feed. The ideal position should be close to the one determined from your design with SimMLA, where any diffraction peaks are smoothed out to a minimum (Supp. Fig. 7).

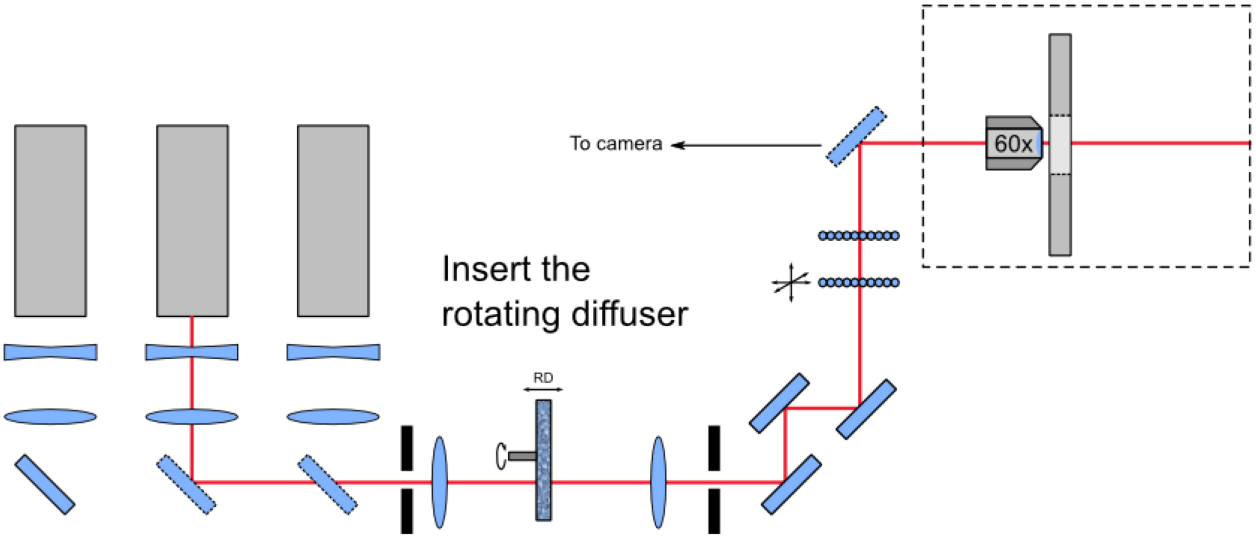

Step 9: Align the microlenses relative one another

Now that everything is in place, slide the first MLA back and forth along the axis and observe the illuminated region in the video stream. Align the transverse position of the first MLA by adjusting its micrometre screws. The MLAs will be aligned relative to one another when sliding the MLA back and forth along the axis does not significantly change the position of the centre of the illuminated region or the flatness. Lock the MLA position into place if desired.

If needed, you can make small adjustments to the diffuser and MLA positions to get a nice, flat illumination field. You may also make fine adjustments to the laser dichroics to get a good overlap of the of their excitation profiles. If additional smoothing is required, try introducing a slight defocus to the beam by inserting a long focal length lens close to the dichroic and after the MLA's (Supp. Fig. 12). Additional smoothing is usually only needed for high quality laser beams ($M^2 \leq 1.1$) that create strong diffraction patterns on the sample plane.

Intuitive explanation

To gain a better understanding of how FIFI works, consider Fig. 2 in the main text. An input Gaussian laser beam is focused by a lens, but before it reaches its focus at the lens's focal plane, it encounters the rotating diffuser. Scattering of the beam through the diffuser creates an effective, partially coherent source whose size is equal to the size of the spot on the diffuser. The divergence of this new beam depends on the beam's original divergence before the diffuser and the diffuser's roughness; high efficiency diffusers are best because they only increase the divergence of the beam by a few degrees (Methods), which allows the light to be efficiently collected by the collimating lens and delivered to the MLA's downstream. If the diffuser is too rough, the light will scatter into large directions and not be efficiently collected by the second telescope lens.

The second, or collimating lens, simply collects the light from the partially-spatially coherent effective source on the diffuser and directs it onto the first MLA. It must have an appropriate focal length to avoid overfilling the aperture of the MLA (whose square sides have lengths D_{MLA}), which would lead to both loss of light and possibly uniformity on the sample (Fig. 3c, Supp. Fig. 5c). The collimating lens focal length and source size together determine the divergence of the light through the system and how easily the light can be squeezed through the MLA and objective apertures.

In traditional Köhler illumination, all the rays that emanate from a single point in the source plane are evenly distributed across the sample plane. This indeed smooths the irradiance profile of the illumination if there is a strong position-dependence of the source irradiance as there is, for example, when the source is a bulb filament. However, the uniformity of traditional Köhler illumination will be degraded if there is a strong *angular* dependence on the source light intensity because there is a one-to-one (instead of one-to-many) mapping between rays that leave the source at approximately the same angle and a single point on the sample.

FIFI—and the Köhler integrator more generally—overcomes this limitation by mapping rays spanning multiple solid angles evenly across the sample plane while maintaining the one-to-many relationship between source points and sample points. Referring to Fig. 2 in the main text, one can see that rays that emanate from a single point on the source and that fill the entrance pupil of one of the lenslets in the first MLA are evenly distributed across the sample. For example, the solid rays come from the same on-axis point and completely fill the entrance pupil of the top-most lenslet in the first MLA. These rays are directed by the system to completely cover the same region in the sample as the dashed ray bundle, which come from a different source point, propagate at different angles than the solid rays, and completely fill a different lenslet entrance pupil. FIFI therefore makes use of multiple Köhler illumination channels in parallel to smooth out spatial and angular variations in the source.

Typical treatments of Köhler integrator design with laser illumination consider only the special case of plane wave input and the objective lens located immediately after the second MLA, possessing an aperture of infinite size. The design equations for this case are simple and have been elaborated in detail for some time[4,5]. FIFI, on the other hand, must account for an extended, partially coherent source, an input beam on the first MLA that has a non-zero divergence, and an objective lens placed at a large offset to the second MLA and possessing an aperture of severely limiting size. We found the geometrical optics design equations[4] useful for an initial illuminator design, but the wave optics simulation developed in this manuscript was needed to accurately predict the power loss and uniformity caused by these deviations from the special case dealt with in previous works.

Ease of Use and Advantages

One of the advantages of using FIFI is that it is relatively easy to align once the design parameters have been calculated. The microlenses may be placed anywhere on the optics axis between the collimating lens and the dichroic preceding the objective

(Fig. 2), so long as the beam does not overfill the objective back aperture. This is by virtue of the fact that the second microlens array (MLA) images the lenslets in the first array to infinity, creating an infinity space between the MLAs and the objective that is insensitive to the exact axial position of the MLA pair. It is also not necessary to ensure a precise transverse placement of the MLA pair with respect to the optical axis; however, the MLA's should still be aligned with respect to one another to within a few tens of microns (see Step 9 above). Additionally, uniformity of the illumination is not compromised by relative errors of a few millimetres in the MLA spacing; instead, we gain a feature in that the size of the illumination can be continuously varied (Supp. Fig. 13) over an order of magnitude simply by changing the spacing by up to one centimetre. The flexibility in the MLA placement means that the system does not go out of alignment easily. In fact, in our lab the MLA's are mounted in a way that lets users reposition by them by hand to change the size of the illuminated field in a matter of seconds; this is done frequently and does not require us to realign the system. Realignments of the whole system typically occur once every few months.

Another advantage of FIFI is that it can easily handle the range of wavelengths used in SMLM without any modification. In this work we illuminated the sample with 405 nm, 642 nm, and 750 nm laser light. Any transverse chromatic aberration would be inconsequential since any shift should be on the order of roughly 0.5 µm over the 100 µm FOV, an error of only 0.5%. Furthermore, axial chromatic aberration probably causes a small relative defocus between focal planes of the illumination, but also appears to be inconsequential (Supp. Fig. 13).

One alternative to FIFI for creating a flat laser illumination profile could be to image a light source with flat output radiance like a multimode fibre onto the sample in a critical illumination geometry[6]. (In critical illumination, the output of the illumination source is imaged directly onto the sample.) In particular, the output of the multimode fibre should be first magnified onto an intermediate plane conjugate to the sample, and then imaged to infinity with a field lens before being focused onto the sample through the objective. Here, all distances between optics lying outside the infinity space must satisfy the image formation equations. The same holds for engineered diffusers that require a Fourier lens to translate the flat angular spectrum into a top-hat irradiance distribution in an intermediate plane. (The scattering angles of such diffusers are similar to the numerical apertures of multi-mode fibres, so they would likely require re-imaging on intermediate planes to avoid overfilling the objective back apertures.) Changing the size of the illumination profile in such a setup would probably require changing either the fibre or the lenses and their positions. Alternatively a zoom lens could be introduced to resize the illumination spot, but we have not tried this ourselves to know how well it would work. In comparison, FIFI avoids the need for fibre coupling or re-imaging onto intermediate planes, and the illumination spot is easily resized by a coarse axial translation of one of the MLA's (Supp. Fig. 13).

Finally, any laser illumination method that generates a flat profile needs to be randomized to avoid the deleterious effects of speckle. In FIFI, this is done with the rotating diffuser and through the selection and placement of the optics; with the multimode fibre, one needs to shake the fibre or pass the output through a rotating diffuser at rates higher than the frame rate of the camera. In this regard, neither approach probably offers a clear advantage.

A disadvantage of FIFI is the relatively slow roll off of the area outside the flat-illuminated region (Supp. Fig. 7-9), which occurs over a range of between 10 or 20 μm. This is a diffraction effect coming from the small Fresnel number of the microlenses and probably cannot be improved much without decreasing the size of the illuminated spot.

To summarize, we find that the advantages of FIFI to be:

1. robust to misalignment
2. wavelength insensitive over the optical range
3. easily resized illumination spot
4. low losses of approximately 10—20% (Supp. Text)

4. THEORY FOR FIELD-DEPENDENT SWITCHING RATES

Direct-STORM exploits the existence of reversible, long-lived, non-fluorescent OFF-states wherein fluorescent molecules may reside before returning to a fluorescent ON-state either stochastically or upon absorption by a UV photon[7,8]. Though the details are dye-specific, their photophysical dynamics may be simplified to a three-state system possessing ON, OFF, and bleached states[7,8]. Transitions to the ON and OFF states occur with rate constants k_{ON} and k_{OFF}, respectively. The non-fluorescent bleached state is conceptually different from the OFF state because transitions to it are irreversible. With a suitable choice of laser irradiances and/or concentrations of reducing agents in the imaging buffer, the rate constants between the three states may be made to differ by an order of magnitude or more, increasing with $k_{OFF} \leq k_{ON} \leq k_{bleach}$[8].

When the bleaching time can be made sufficiently long relative to the acquisition time, then the dye is described by a simple, two-state system whose steady state solution is

$$\frac{k_{OFF}}{k_{ON}} = \frac{N_{OFF}}{N_{ON}}$$

with $N_{OFF} + N_{ON} = N$ representing the populations of the OFF and ON states per diffraction-limited area. To precisely localize single fluorescent molecules, one or fewer molecules should be in the ON state per diffraction-limited area at any given time, so that $N_{ON} = 1$ and $N_{OFF} \approx N$. The criterion for STORM imaging is then

$$\frac{k_{OFF}}{k_{ON}} \geq N$$

which means that the ratio of the off-rate to the on-rate must exceed the local density of fluorophores. Furthermore, the transition rate to the OFF state varies linearly with the laser irradiance[7]. Using I for the irradiance, this allows us to write

$$cI \geq N$$

where c is a proportionality constant. Thus, the local excitation irradiance in a diffraction limited area must be greater than the density of fluorophores to within a constant factor. If the irradiance is too high, then the acquisition must be made unnecessarily long to record a large enough density of localisations to achieve a given resolution in the final image. If the irradiance is too low, too many fluorophores will emit in a region at once, preventing their accurate localisation.

When imaging cells, organelles, or macromolecular clusters, the local density of fluorophores in the sample will vary spatially with the density of the target species. Over length scales spanning a single cell or more, however, we can attribute to the sample an effective density of fluorophores that is set by the most densely labelled structure we wish to image. This density dictates the minimum required irradiance to perform STORM imaging, and is illustrated in Fig. 1e of the main text.

In PALM, the fluorophores that are imaged are usually fluorescent proteins. The photophysical mechanisms that describe blinking are different than dyes and vary fluorophore-to-fluorophore. Just like dyes, though, fluorescent proteins may be still be abstracted into ON, OFF, and bleached states with at least one rate constant that depends on the laser irradiance. A flat excitation profile is therefore advantageous for PALM as well.

5. FIELD-DEPENDENT DIRECT STORM SIMULATIONS

Motivation

As a follow up to the preceding discussion, one may ask “How flat should the illumination be?” when assessing the quality of the epi-illumination in a standard SMLM experiment. Historically, SMLM measurements that were taken in epi-illumination were confined to the centre of the field of view (FOV) where the spatial roll-off in irradiance on the sample was negligible, thereby avoiding this question. In this section, we explore the effects of a field-dependent illumination in the two special cases discussed in the main text: Gaussian beam illumination and flat illumination. Extension to more complicated illumination patterns should easily follow from these two cases.

The required flatness for widefield SMLM epi-illumination depends on multiple parameters, the most important of which are (1) the peak irradiance on the sample, (2) the local density of fluorophores, and (3) the available laser power. Given different values for each of these, the flatness requirements will change, sometimes significantly. For these reasons, we cannot produce a single value or easily identify a quantity such as the gradient of the irradiance that will suffice for determining the outcome of a SMLM experiment. Instead, to better understand the influence of these parameters and the dependence of the reconstruction on the field-dependent illumination, we simulated direct STORM experiments using Gaussian beam illumination under conditions similar to those encountered in the lab.

Under Gaussian beam illumination, the radial dependence of the irradiance (which has units of power per area) on the sample follows a simple Gaussian expression:

$$I(r) = I_0 e^{-2r^2/w_0^2}$$

Here, I_0 is the on-axis irradiance and the beam waist radius w_0 is the distance from the axis where the irradiance drops to a fraction $I/I_0 \approx 0.14$ of the on-axis value. The power carried by a fraction of the beam that passes through a circular area on the sample centred on the axis with radius r is

$$P(r) = P_0\left(1 - e^{-2r^2/w_0^2}\right)$$

with the total beam power given by a two-dimensional integral over the irradiance:

$$P_0 = \left(\frac{\pi w_0^2}{2}\right) I_0$$

From the above expressions, approximately 86% of the power carried by the Gaussian laser beam lies within one beam waist radius; 99% lies within 1.5 beam waist radii. The on-axis irradiance I_0 and the total beam power P_0 are related to one another through the waist radius. Most importantly, and for a fixed beam power, increasing the waist radius by a factor x decreases the on-axis irradiance by a factor x^2.

In SMLM, rate constants for switching fluorescent molecules between emitting and reversible, non-emitting states usually depend on the local laser irradiance. For example, in direct STORM, the transition rate constant k_{off} from the emitting state to the long-lived dark state of a fluorescent dye molecule is linearly proportional to the laser irradiance[8]. Hence, the molecules at a distance of one waist radius from the axis will transition to the dark state at a rate that is 0.14 times as large as the molecules in the centre of the beam.

The relationship between the transition rate constant k_{off} (or equivalently the on-time) and the laser irradiance was estimated from single molecule blinking tests and the fact that $k_{OFF} = 0$ when the irradiance is zero[7]. To perform the tests, we dispersed a dilute solution of AlexaFluor 647 dye onto a coverslip and imaged the individual dye molecules under a flat-illuminated area of $110 \times 110\ \mu m^2$ and $5\ kW/cm^2$ of 642 nm light in the same buffer as reported in the manuscript. Raw localisations from within the same 90 nm diameter area were temporally merged with a dark time of zero; doing so produced a distribution of molecule on-times with a mean on-time of 2.8 frames = 28 ms. This led to a proportionality constant of

$$c = \frac{1}{(0.028\, sec)(5\ kW/cm^2)} = 7.14\ cm^2/kJ$$

between the on-time (which was a simulation input), and the irradiance (which is what we wanted to vary).

Simulation Details

We used SuReSim Version 0.5.1 with all default parameters, except for those listed in the table below. As a ground truth structure, we used a $1 \times 1\, \mu m^2$ square grid with epitopes placed every $1 \times 1\, nm^2$ and varied the label density accordingly. Simulated on-times were 1, 0.3333, 0.1000, 0.0333, 0.0100, 0.0033 seconds, corresponding to irradiances of 0.14, 0.42, 1.4, 4.2, 14, and 42 kW/cm^2.

Parameter	**Value**
Binding Angle [deg]	0
Label Epitope Distance [nm]	0.1
Allow bleaching:	Checked

Bleach constant:	2.231e-5
Background label [um^-3]:	0
Pixel to Nm Ratio	108
Frame Rate [s^-1]	100
Readout Noise [DN]	1.42
Constant Offset	100
EM Gain	1
Quantum Efficiency (Note there is a bug in the GUI: 0.7 = 70%)	0.7
Electrons/DN	0.49
Numerical Aperture	1.4
Wavelength [nm]	670
Defocus [nm]	400
Focus [nm]	0

For the localisation analysis and comparison to the ground truth, we used ThunderSTORM 1.3-2014-11-08. For the camera setup, we used:

Parameter	**Value**
Pixel size [nm]	108
Photoelectrons per A/D count	0.49
Base level [A/D] counts	90
EM Gain	Unchecked

For the localisation analysis, we used the following parameters:

Parameter	**Value**
Filter	Wavelet filter (B-Spline)
B-Spline order	3.0
B-Spline scale	2.0
Approx. loc. of molecules: Method	Local maximum
Peak intensity threshold	2*std(Wave.F1)
Connectivity	8-neighborhood
Sub-pixel loc. of molecules: Method	PSF: Gaussian
Fitting radius [px]	3
Fitting method	Weighted Least Squares
Initial sigma [px]	1.5
Multi-emitter analysis	Not enabled

The comparison to the ground truth was also performed using the Performance Evaluation feature of ThunderSTORM and a xy radius of 50 nm.

Bleaching in the simulations was set to a constant because we did not possess accurate data to use for the irradiance-dependent bleaching rates. With a fresh imaging buffer, the effects of bleaching over the length of the simulations (10,000 frames at 100 fps = 100 seconds) is negligible. Furthermore, similar investigations found a relatively small bleaching rate for even higher irradiances in STORM[9]. We expect to find a smaller number of localisations in the beam centre during STORM experiments lasting longer than about 100 seconds due to a higher bleaching rate there. In PALM experiments, the field-dependent bleaching rate likely cannot be ignored as we do here.

In the simulations, we uniformly and randomly labelled $1 \times 1\ \mu m^2$ flat surfaces that were perpendicular to the optics axis with four different densities of fluorophores: 100, 300, 1000, and 3000 μm^{-2}. For each fluorophore density, we next generated raw image stacks consisting of 10,000 frames each using the SuReSim simulation package[10]. Values for the irradiance of 0.14, 0.42, 1.4, 4.2, 14, and 42 kW/cm^2 were simulated separately by adjusting the mean fluorophore on-time and applying an experimentally determined constant of proportionality between the on-time and the irradiance (see the above section for details). Localisations from the raw image stacks were then computed in ThunderSTORM[11]. These raw localisations were filtered to remove those with a localisation uncertainty greater than 20 nm and a chi-squared fit value greater than 250. These are the same filters applied to the data in Fig. 1 of the main manuscript and are commonly used values by us to reject poor localisations. Localisations were not merged to avoid the introduction of counting artefacts when the density of on-state emitters was high.

The sets of localisations were next compared to the ground truth fluorophore positions generated by SuReSim using three computed quantities: the density of detected localisations, the precision, and the recall. The density of detected localisations is the sum of all true positive and false positive localisations, or $TP + FP$. (A true positive is a detected localisation in the same frame as a ground truth molecule that also lies within a circle of a chosen radius that is centred on that ground truth position; in this case the radius was set to a somewhat generous 50 nm.) The precision (not to be confused with the *localisation* precision) is the ratio of true positives to all detected localisations $TP/(TP + FP)$, and the recall is the ratio of true positives to the sum of true positives and false negatives, $TP/(TP + FN)$. The results of the simulations are plotted in Supp. Fig. 3. Each row contains the results for a different on-axis irradiance as specified by the labels in the figure. The x-axis for each plot represents the distance from the Gaussian beam centre in units of the beam waist radii and were determined from the expression for the beam irradiance:

$$\frac{r}{w_0} = 0.7071\sqrt{-\ln\left(\frac{I}{I_0}\right)}$$

Results for the different peak irradiances were obtained simply by removing all data corresponding to irradiances above I_0 and shifting and rescaling the x-axis appropriately, which explains the decreasing number of data points as the peak irradiance decreases.

Direct STORM Simulation Results

Though the results are quite complex, we can begin to understand them by identifying a few important features. First, the density of detected localisations can vary by a factor of two or more across the width of the laser beam and depends both on the density of fluorophores and the on-axis irradiance. The only situation in which it varied by no more than roughly 20% across the entire beam diameter was for the case of $I_0 = 4.2\, kW/cm^2$ and $1000\ fluorophores/\mu m^2$ (Supp. Fig. 3c). Second, the best precisions and recalls are always obtained in the region of the beam where the irradiance is highest. This happens because localisations are more likely to be well-isolated and brighter in these areas, though this same fact leads to a smaller density of localisations. For the somewhat typical irradiance $I_0 = 4.2\, kW/cm^2$ and a somewhat low density of $1000\ fluorophores/\mu m^2$, the precision drops from nearly 100% to only 50% across the beam diameter, although the most significant drop is between the region spanning $0.75w_0$ and w_0. This means that nearly half of all the localisations in this region of the beam were more than 50 nm away from their ground truth positions. It is important to note that this happens even after filtering out localisations with estimated uncertainties that were greater than 20 nm as described above, highlighting the fact that a calculated uncertainty from a localisation algorithm does not necessarily reflect the actual error in a localisation's position.

It is clear that the reconstruction quality of a SMLM image will vary significantly across the illuminated area. It is furthermore clear that the quality measures depend in a non-trivial way on a number of parameters. Yet another important point concerns the largest possible beam size that would satisfy a desired level of precision. For this example consider a laser beam carrying $1\, W$ of power in the sample plane, an on-axis irradiance of $I_0 = 14\ kW/cm^2$ and a sample with a fluorophore density of $1000\, \mu m^{-2}$ (Supp. Fig. 3b). Let's assume that we can tolerate a precision of 90% in our measurements. According to the middle plot in Supp. Fig. 3b, the requirement on the precision can be satisfied in the region within one beam waist radius. The size of a laser beam with these parameters is obtained from the expression above for the total beam power:

$$w_0 = \sqrt{\frac{2P_0}{\pi I_0}} = \sqrt{\frac{2\ (1\ W)}{\pi(1.4 \times 10^4\ \ W/cm^2)}} \approx 67\ \mu m$$

Under this illumination, just under 6000 localisations will be detected in the beam centre versus about 9000 detected localisations at the edge, and between 50% and 60% of all the possible localisations will actually be detected.

How does this compare to a flat illumination profile? In terms of the reconstruction quality, every curve in Supp. Fig. 3 would be independent of the beam position for flat-illuminated samples (up to the edge of the beam, of course); any variation in the curves as a function of position in a real measurement would be due to either noise or sample heterogeneities, but not the illumination. The largest possible size of the flat-illuminated area would depend on the power required to produce an irradiance that leads, again in this example, to a precision of 90%. Here, the minimum required irradiance occurs at the beam waist and is $I(w_0) = I_0 e^{-2w_0^2/w_0^2} = (14\ \ kW/cm^2) \times e^{-2} \approx 1.9\ \ kW/cm^2$. The side-length of a square region containing 1 W of power at this irradiance is

$$x = \sqrt{\frac{1\ W}{1900\ \ W/cm^2}} \approx 230\ \mu m$$

which is about the same size as a full $2048 \times 2048\ pixel^2$ sCMOS camera chip with a 110 nm sample-space pixel size. In fact, and in this example, a flat illumination will cover an area that is $(230\ \mu m)^2/\pi(67\ \mu m)^2 = 3.75$ times larger than the Gaussian beam of the equivalent power while still meeting the precision requirements of the measurement.

One may propose simply buying a more powerful laser and expanding the Gaussian laser beam as a simpler means for imaging a larger FOV than creating a flat illumination. However, the unfavourable scaling of the required power with the beam radius $P_0 \sim w_0^2$ would mean that the input power in the above example should also be increased by a factor of 3.75 to $P = 3.75\ W$ just to make the beam cover an area equal to the flat-illuminated region and still satisfy the precision requirements. We should stress that this will be 3.75 W *on the sample*; losses in mirrors, dichroics, the objective, and all other optical elements between the laser and sample would require a laser that outputs probably at least 5 W, which starts to drastically increase the price of the laser. One can appreciate that expanding the Gaussian beam further still so that the irradiance roll-off over this $230\ \times 230\ \mu m^2$ area is small, say only 15% of the maximum, would require totally unrealistic laser powers in excess of 10’s or even 100 *Watts*.

How does this discussion extend to EMCCD cameras, which typically have FOV’s that are at most ~$50 \times 50\ \mu m^2$? In practice, the imaged FOV is usually smaller than this due to limits on the available laser power and longer camera integration times. The FIFI system would still be advantageous for these users to expand their FOV because, aside from providing a more uniform reconstruction, a flat illumination profile makes for a more economical use of the available laser power.

To complete this discussion, we consider the issue of the largest possible Gaussian beam illuminated area relative to the largest flat-field illuminated area assuming a minimum required irradiance I_{min} (see Fig. 1e of the main text) and constant laser power P_0. In this case, we ignore any requirements on uniformity in the illumination and only ask what the area of the largest beams is for the two schemes that has an irradiance at least as large as I_{min}.

In the flat-field case, and for a square illumination region, the largest beam size occurs when the irradiance equals I_{min}:

$$R_f = \frac{1}{2}\sqrt{\frac{P_0}{I_{min}}}$$

Here, R_f is half the length of one of the sides of the region. The radial distance R_g between the beam center and the annular region of the Gaussian beam where the irradiance is equal to I_{min} is found from the equation

$$I_{min} = I_0 e^{-2R_g^2/w_0^2}$$

where again I_0 is the peak irradiance and w_0 is the beam width. When we solve this equation for R_g and use the expression $P_0 = \pi w_0^2 I_0/2$ to eliminate w_0, we obtain the expression

$$R_g = \sqrt{\frac{P_0}{\pi I_0}\ln\left(\frac{I_0}{I_{min}}\right)}$$

This expression is only valid when $I_0 \geq I_{min}$; when the peak irradiance equals the minimum irradiance, we have the case illustrated by the green beam profile in Fig. 1e. Taking the ratio of these two distances gives

$$\frac{R_f}{R_g} = \frac{\sqrt{\pi}}{2}\sqrt{x/\ln x}$$

where $x = I_0/I_{min}$. The above ratio has a minimum of approximately 1.45 when the ratio of the peak to minimum irradiances is approximately 2.7. The corresponding ratio of illuminated areas is $(2 \times 1.45)^2/\pi \approx 2.7$. At its largest, the Gaussian beam spans an area that is only slightly more than one third of the area of the flat-illuminated region.

If the flat-illuminated region carries a factor η less power than the Gaussian scheme—as it would if the losses in the flat illumination were higher—then its largest size would instead be $R_f = 0.5\sqrt{\eta P_0/I_{min}}$. The ratio of the two beam sizes would drop to less than one when the relative efficiency became 0.48 or less. Thus, to take advantage of the larger fields of view, the flat-field scheme should be at least ~50% as efficient as the Gaussian beam illumination scheme; you can afford to lose up to half the power.

We can summarize the preceding discussion as follows:

1. Both the size and the quality of a SMLM reconstruction depend on a number of factors, including the peak irradiance on the sample, the density of fluorophores, and the amount of laser power available.
2. A Gaussian beam causes significant variation in the quality of the reconstructed localisations across the FOV in a SMLM experiment.
3. Flat illumination is a more economical use of the available laser power, allowing for an illuminated area that is at least 2.7 times larger than a Gaussian beam of the same power and 3 to 4 times larger when minimizing any dependence of the quality of the reconstruction on the illumination.
4. Ignoring requirements on illumination uniformity, the flat-field scheme produces larger fields of view when it is at least 50% as efficient as the Gaussian illumination scheme.

6. WAVE OPTICS THEORY FOR THE KÖHLER INTEGRATOR

Geometrical optics and wave optical modelling of a Köhler-integrator has been developed by a number of authors for both fully coherent and incoherent sources and with the microlens arrays (MLA's) acting as the sole limiting apertures[4,12–14]. In this section, we develop the wave optics theory necessary to predict the 1D irradiance profile on the sample as a function of the design parameters illustrated in Fig. 2 of the main text. This theory accounts for both the partial spatial coherence of the source created by the rotating diffuser and the finite apertures in the illumination train of the microscope, which are typically neglected in the literature. These factors are necessary for assessing the quality of the two properties that are required of the illuminator: homogeneity of the irradiance on the sample and efficient throughput of the laser beam power. The theory does not account for losses due to scattering at the lenslet interfaces in the MLA's or aberrations in the lenslets themselves. It can be easily extended to 2D, but is developed in 1D due to spatial sampling limitations in its computational implementation.

With regards to Fig. 2 in the main text, a collimated, monochromatic, scalar Gaussian beam with wavelength λ is input into the illuminator along the z-axis and, in the absence of the diffuser, would be focused to a waist radius $w_0 = \sqrt{2}\sigma$ in the focal plane of the first telescope lens with σ representing the standard deviation of the Gaussian. The Gaussian beam is described mathematically as

$$g(x,z) = A\frac{w_0}{w(z)}e^{-x^2/w(z)^2}e^{\left[j\left(kz+kx^2/2R(z)\right)\right]}$$

Here A is the amplitude of the scalar field, $w(z)$ is the beam waist parameter and $R(z)$ is its curvature. The total power carried by this 1D beam is independent of the spatial coordinates and is represented by

$$P = \frac{1}{Z_0}\int_{-\infty}^{\infty} |g(x,z)|^2 dx$$

where $Z_0 \approx 377\Omega$ is the impedance of free-space. Because this is a 1D treatment derived from a separable solution of the Helmholtz wave equation, A has units of $Volts/\sqrt{\mu m}$.

Prior to the beam waist, a high-efficiency, rotating diffuser is inserted into the beam path at an offset Δr from the focal plane. The diffuser's surface is comprised of many small, randomly organized, continuous glass grains whose linear size is on the order of 10 µm. The surface profile can therefore be modelled as a continuous random process $\mathbf{X}(x)$ with a correlation length σ_f equal to the size of a grain and an amplitude variance σ_r. The corresponding phase mask describing the optical properties of the diffuser is

$$t(x) = e^{j\mathbf{X}(x)}$$

A method for generating such a surface profile with a Gaussian power spectrum was described previously in the context of laser beam propagation through a turbulent atmosphere[15]. The value for σ_r that described our diffuser was determined by running several simulations, each with parameters matching our experimental setup except for different values of σ_r. A good value for σ_r was found when the simulated contrast of the fringes produced by the grating pattern matched the experimental contrast.

Setting the common focal planes of the two telescope lenses as the $z = 0$ plane, the scalar field at the surface of the diffuser is given by

$$u_{in}(x) = t(x)g(x, \Delta r)$$

When the diffuser lies close to the focal plane, the size of the laser beam will be small relative to the diffuser's grain width σ_f, so the phase of the beam is minimally perturbed by the diffuser (Supp. Fig. 10). As the diffuser is offset from the focal plane by a distance greater than the beam's Rayleigh range, the cross sectional area of the beam will intercept a greater and greater number of randomly distributed grains on the diffuser, leading to a random spatial phase distortion that grows with the offset. Increasing the offset therefore increases the size of partially coherent extended source. This input field is propagated to the back focal place of the second telescope lens and is represented as $u_0(x_0)$.

For large enough focal lengths f_c such that the paraxial approximation is valid, the field in the front focal plane of second telescope lens is proportional the Fourier transform $\mathcal{F}$ of the extended source[16]

$$\frac{1}{\sqrt{\lambda f_c}} \int_{-\infty}^{\infty} \left[u_0(x_0) e^{-j2\pi x_0 x/\lambda f_c}\right] dx_0 = \frac{1}{\sqrt{\lambda f_c}} \mathcal{F}[u_0](x)$$

This field is propagated away from the telescope lens's front focal plane over a distance $L_1 - f_c$ where it becomes $u_1(x_1)$ and encounters the first MLA. Each MLA is comprised of a regular grid of N identical spherical lenslets of focal length f_{MLA} and spaced by a period p. Owing to their rectangular apertures, each lenslets samples the field with rectangular sampling window

$$\mathrm{rect}\left(\frac{x - mp}{p}\right)$$

where m is an integer between $-\frac{N-1}{2}$ and $\frac{N-1}{2}$ for odd N. The $\mathrm{rect}\left(\frac{x}{a}\right)$ function is unity between $-\frac{a}{2}$ and $\frac{a}{2}$ and zero elsewhere. The lenslets create a multi-focal spot array of the sampled field $u_1(x_1)$ in the plane of the second MLA. Owing to the fact that the curvatures of the lenslets in the second array are identical to the ones in the first, the quadratic phase term imparted by the first array lenslets is cancelled[12,16], leading to the expression

$$u_2(x_2) = \frac{1}{\sqrt{\lambda f_{MLA}}} \times$$

$$\sum\nolimits_m \left\{ \int_{-\infty}^{\infty} u_1(x_1) \mathrm{rect}\left(\frac{x_1 - mp}{p}\right) \exp\left[-j \frac{2\pi}{\lambda f_{MLA}} (x_1 - mp)(x_2 + mp)\right] dx_1 \right\} \mathrm{rect}\left(\frac{x_2 - mp}{p}\right)$$

Here it is assumed that the focused spot on the second MLA is much smaller than the size p of the lenslets, which means that there is no cross-talk between lenslets that do not lie on a line parallel to the optics axis. This is a reasonable assumption when the field varies slowly over the aperture of a lenslet in the first MLA.

This field is propagated again over a distance L_2 where it encounters the aperture in the back focal plane (BFP) of the microscope objective, $\mathrm{rect}\left(\frac{x}{D_{BFP}}\right)$. Infinity-corrected objectives are typically designed to meet the Abbe sine criterion over a large angular range. For this reason, the field in the sample plane may be written as the Fourier transform of the field in the BFP

$$u_4(x_4) = \frac{1}{\sqrt{\lambda f_{OBJ}}} \mathcal{F}[u_3(x_3)](x_4)$$

even though the light propagates at large angles.

7. REFERENCES

1. Thompson, R. E., Larson, D. R. & Webb, W. W. Precise nanometer localization analysis for individual fluorescent probes. *Biophys. J.* **82,** 2775–83 (2002).
2. Huang, F., Schwartz, S. L., Byars, J. M. & Lidke, K. A. Simultaneous multiple-emitter fitting for single molecule super-resolution imaging. *Biomed. Opt. Express* **2,** 1377–93 (2011).
3. Huang, F. *et al.* Video-rate nanoscopy using sCMOS camera-specific single-molecule localization algorithms. *Nat. Methods* **10,** 653–8 (2013).
4. Völkel, R. & Weible, K. J. Laser Beam Homogenizing: Limitations and Constraints. *Proc. SPIE* **7102,** 71020J–71020J–12 (2008).
5. Brown, D. M., Dickey, F. M. & Weichman, L. S. in *Laser Beam Shaping: Theory and Techniques* (eds. Dickey, F. M. & Holswade, S. C.) (CRC Press, 2000). doi:10.1201/9780824741631.ch7
6. Cooper, D. J. F. Imaging distal end of multimode fiber. (2014). at <http://www.google.com/patents/US8922887>
7. Heilemann, M. *et al.* Subdiffraction-resolution fluorescence imaging with conventional fluorescent probes. *Angew. Chem. Int. Ed. Engl.* **47,** 6172–6 (2008).
8. van de Linde, S. *et al.* Direct stochastic optical reconstruction microscopy with standard fluorescent probes. *Nat. Protoc.* **6,** 991–1009 (2011).
9. Lin, Y. *et al.* Quantifying and optimizing single-molecule switching nanoscopy at high speeds. *PLoS One* **10,** e0128135 (2015).
10. Venkataramani, V., Herrmannsdörfer, F., Heilemann, M. & Kuner, T. SuReSim: simulating localization microscopy experiments from ground truth models. *Nat.*

Methods **13,** 319–321 (2016).

11. Ovesný, M., Křížek, P., Borkovec, J., Svindrych, Z. & Hagen, G. M. ThunderSTORM: a comprehensive ImageJ plug-in for PALM and STORM data analysis and super-resolution imaging. *Bioinformatics* **30,** 2389–90 (2014).
12. Streibl, N., Nölscher, U., Jahns, J. & Walker, S. Array generation with lenslet arrays. *Appl. Opt.* **30,** 2739–42 (1991).
13. Wippermann, F., Zeitner, U.-D., Dannberg, P., Bräuer, A. & Sinzinger, S. Beam homogenizers based on chirped microlens arrays. *Opt. Express* **15,** 6218 (2007).
14. Büttner, A. & Zeitner, U. D. Wave optical analysis of light-emitting diode beam shaping using microlens arrays. *Opt. Eng.* **41,** 2393 (2002).
15. Xiao, X. & Voelz, D. Wave optics simulation approach for partial spatially coherent beams. *Opt. Express* **14,** 6986 (2006).
16. Goodman, J. W. *Introduction to Fourier Optics*. (Roberts and Company Publishers, 2005). at <https://books.google.ch/books/about/Introduction_to_Fourier_Optics.html?id=ow5xs_Rtt9AC&pgis=1>